
A Stability Benchmark of Generative Regularizers for Inverse Problems

Alexander Denker*

Helmholtz Imaging, Deutsches Elektronen-Synchrotron DESY, Germany
alexander.denker@desy.de

Johannes Hertrich

ENS Paris & Inria, France
johannes.hertrich@ens.fr

Sebastian Neumayer

Chemnitz University of Technology, Germany
sebastian.neumayer@math.tu-chemnitz.de

Abstract

Generative (diffusion) priors demonstrate remarkable performance in addressing inverse problems in imaging. Yet, for scientific and medical imaging, it is crucial that reconstruction techniques remain stable and reliable under imperfect settings. Typical definitions of stability encompass the notion of “convergent regularization”, robustness to out-of-distribution data, and to inaccuracies in the forward operator or noise model. We evaluate these properties numerically. Furthermore, we benchmark generative approaches against modern optimization-based methods inspired by the widely used variational techniques. Our results give insights for which settings and applications generative priors can deliver state-of-the-art reconstructions, and on those in which they fall short or may even be problematic.

1 Introduction

The search for powerful reconstruction methods is one of the key challenges in computational imaging [Arridge et al., 2019, Ongie et al., 2020, Kiss et al., 2025]. Over the last years, several papers proposed reconstruction methods based on generative models (often called generative priors), see, e.g., Chung et al. [2023], Mardani et al. [2024], Martin et al. [2025], Song et al. [2022], Webber and Reader [2024], Wu et al. [2024]. While these show impressive results in certain settings, their performance is mostly benchmarked on photo-realistic images and tasks such as inpainting, deblurring or super-resolution.

On the other hand, major applications areas of image reconstruction techniques lie in scientific and medical imaging, where fundamentally different challenges and objectives appear compared to photo-realistic image reconstruction. In particular, we have the following key aspects.

1. **Out-of-distribution data:** For photo-realistic imaging, large training datasets that closely match the test distribution are readily available. In contrast, scientific and medical applications typically have only limited training data that matches the desired evaluation setting. Consequently, models are often trained on generic datasets. This makes the ability to generalize to (mildly) out-of-distribution (OOD) data a key factor when designing reconstruction methods in these domains.
2. **Non-generative tasks:** Generative priors are typically evaluated on tasks such as large-area inpainting, conditional generation, or extreme super-resolution, where substantial portions of the original information are missing and must be “recreated”. In contrast, the measurement setup in scientific and medical imaging is usually designed such that the relevant information is faithfully (or at least reasonably) captured. In particular, there should not remain ambiguity given the data. Thus, the primary challenge is usually a low signal-to-noise ratio.

*Work done while at University College London.

3. **Quality assessment:** In photo-realistic imaging, perceptual metrics like LPIPS or FID became very popular, as they measure the similarity of generated features to the ones in the training set. For scientific and medical imaging, the appearance of realistic-looking structures not supported by the data is instead viewed as highly problematic. The primary objective is to reconstruct images while staying faithful to the data. If there is ambiguity, it should be (to some extent) also visible in the reconstruction. Thus, perceptual metrics are only of limited importance.

In this paper, we investigate to which extent the popular diffusion priors (which are a subclass of generative priors) can handle these challenges. Moreover, we investigate how well they compete in this regard with modern learned regularizers. We consider such a study highly relevant since recent benchmarks, for example Shi et al. [2026], find that in certain realistic settings a large number of diffusion priors are not even competitive to simple regularizers such as total variation (TV) [Rudin et al., 1992]. At the same time, other works, for example Jia et al. [2026], attribute strong generalization capabilities to diffusion priors. Moreover, neither of these benchmarks compares diffusion-based approaches with other modern reconstruction methods like learned regularizers [Habring and Holler, 2024, Hertrich et al., 2026] or plug-and-play schemes [Venkatakrisnan et al., 2013, Hurault, 2023, Kamilov et al., 2023].

To study these questions systematically, we consider a linear inverse problem

$$\mathbf{y} = \mathbf{A}\mathbf{x} + \boldsymbol{\eta}, \quad (1)$$

where $\mathbf{x} \in \mathbb{R}^n$ is the unknown image, $\mathbf{y} \in \mathbb{R}^m$ the measurement, $\mathbf{A} \in \mathbb{R}^{m \times n}$ the computational imaging model, and $\boldsymbol{\eta}$ additive noise accounting for inaccuracies and model mismatch. To distinguish the different settings, we first classify the inverse problem (1) according to its degeneracy.

1. **Type I (Ill-conditioned):** The forward operator \mathbf{A} is injective and one has to mainly compensate for the noise $\boldsymbol{\eta}$, which might be amplified by small singular values of \mathbf{A} .
2. **Type II (Identifiable):** The forward operator \mathbf{A} has a non-trivial nullspace, but (1) still admits a unique plausible solution (identifiable by incorporating prior knowledge).
3. **Type III (Non-identifiable):** The problem (1) admits several plausible solutions among which a selection is necessary.

Scientific and medical imaging mainly focuses on ill-conditioned and identifiable problems. There, we expect from a reasonable reconstruction method $R_\alpha: \mathbb{R}^m \rightarrow \mathbb{R}^n$ with regularization strength α (which can be seen as tunable hyperparameter) that it fulfills the following properties.

1. **Performance:** There exists a regularization strength α (depending on the expected corruption $\delta^2 = \mathbb{E}[\|\boldsymbol{\eta}\|^2]$) such that the average reconstruction error $\mathbb{E}_{\mathbf{x}, \mathbf{y}}[\|R_\alpha(\mathbf{y}) - \mathbf{x}\|^2]$ is small.
2. **Data Consistency:** $\|\mathbf{A}R_\alpha(\mathbf{y}) - \mathbf{y}\|^2 \lesssim \delta^2$, namely that it remains faithful to the data.
3. **Stability:** $\|R_\alpha(\mathbf{y}_1) - R_\alpha(\mathbf{y}_2)\| \rightarrow 0$ whenever $\mathbf{y}_2 \rightarrow \mathbf{y}_1$.
4. **Generalization:** The method should still work for slightly OOD data, mismatched forward operators \mathbf{A} and altered noise models.

In the classical inverse problems literature [Engl et al., 1996], these properties are closely related to the notion of *convergent regularization*. This notion entails that there exists a schedule $\alpha(\delta)$, depending on the misfit $\delta^2 = \mathbb{E}[\|\boldsymbol{\eta}\|^2]$, such that $R_{\alpha(\delta)}(\mathbf{A}\mathbf{x} + \boldsymbol{\eta})$ converges to the (projected) ground truth $\mathbf{A}^\dagger \mathbf{A}\mathbf{x}$ as $\delta \rightarrow 0$. While this property is hard to prove in practice, it holds true for some plug-and-play algorithms [Ebner and Haltmeier, 2024, Hauptmann et al., 2025] and for some learned regularizers [Neumayer and Altekrüger, 2025]. A counterpart to this notion in the Bayesian framework is the Bernstein–von Mises theorem [Doob, 1949, Van der Vaart, 2000], which states that the posterior distribution concentrates on the likelihood when the amount of available information grows.

Outline and Contributions We start in Section 2 by classifying linear inverse problems. Then, we give in Section 3 a brief overview of the deployed generative and diffusion-based methods (DiffPIR [Zhu et al., 2023], DMPlug [Wang et al., 2024], DPS [Chung et al., 2023], RED-diff [Mardani et al., 2024] and PnP-flow [Martin et al., 2025]), and the learned regularizers (WCRR [Goujon et al., 2024] and LSR [Hurault et al., 2022, Zou et al., 2023]). In Section 4, we benchmark these methods for medical imaging, specifically on computed tomography (CT). In particular, we investigate the influence of the training data and the robustness against OOD observations and model mismatch. A similar study for natural images is deferred to Appendix A. Based on the obtained results, we discuss in Section 5 to which extent diffusion-based approaches fulfill the desirable properties of reconstruction methods outlined above, and how well they compete against variational methods.

The conclusions drawn in Section 5 vary across diffusion priors, but their overall tendency can be summarized as follows:

The high model capacity of diffusion priors makes them sensitive to distribution shifts. In scientific applications, this sensitivity can lead to deceptive hallucinations. By contrast, lightweight variational methods tend to generalize more robustly and emphasize data consistency, making them more reliable for scientific and medical imaging tasks.

Related work Recent benchmarks for diffusion-based reconstructions include INVERSEBENCH [Zheng et al., 2025] and DM4CT [Shi et al., 2026]. A key finding of INVERSEBENCH is that diffusion priors exhibit a strong bias toward the training distribution and often fail to recover *unexpected* OOD features in the test data. Moreover, the CT-specific benchmark DM4CT reports that the simple TV regularizer is often highly competitive with diffusion priors in type I and II settings. While our focus is on point reconstruction, other benchmarks [Crafts and Villa, 2025, Qiu et al., 2026, Zach et al., 2026] investigate diffusion-based methods for posterior sampling. In contrast to these works, we systematically study the stability properties of diffusion priors and include comparisons to learned regularizers. Moreover, based on our experimental findings, we then discuss *when* and *why* generative priors are actually beneficial.

2 Classification of Linear Inverse Problems

The effectiveness of a reconstruction method depends heavily on the inverse problem (1) that we want to solve. A key consideration is how the operator \mathbf{A} interacts with the manifold \mathcal{M} of plausible images. Instead of a rigid classification, one should think of inverse problems along a spectrum of difficulty, characterised by how much semantically meaningful information is missing.

Among all plausible images in \mathcal{M} , we focus on those consistent with the data \mathbf{y} , namely the set $\mathcal{X}_{\mathbf{y}}^{\delta} = \{\mathbf{x} : \|\mathbf{A}\mathbf{x} - \mathbf{y}\|^2 \leq \delta\}$ for some threshold δ . For the associated set of possible solutions $\mathcal{S}_{\mathbf{y}}^{\delta} = \mathcal{X}_{\mathbf{y}}^{\delta} \cap \mathcal{M}$, it makes sense to consider its diameter $\text{diam}(\mathcal{S}_{\mathbf{y}}^{\delta}) = \sup_{\mathbf{x}_1, \mathbf{x}_2 \in \mathcal{S}_{\mathbf{y}}^{\delta}} \|\mathbf{x}_1 - \mathbf{x}_2\|$ as a measure of hardness. In particular, a small diameter indicates a near-unique reconstruction, while a large one means that there are distinct data-consistent solutions in \mathcal{M} .

Somehow related, we can assess whether a reconstruction method should merely suppress noise, interpolate missing but recoverable structure, or instead generate plausible content that is not supported by the data. From this, we identify three problem types, discussed below and visualized in Figure 1.

Type I (Ill-Conditioned) At the one end of the spectrum, we have injective operators \mathbf{A} , i.e., $N(\mathbf{A}) = \{\mathbf{0}\}$, where the ground truth image is in principle recoverable from the data \mathbf{y} by direct inversion (in the absence of noise). The main difficulty arises from large noise levels or small singular values of \mathbf{A} , which amplify the noise. Thus, the main goal is to stabilize the reconstruction process while preserving the information contained in the data \mathbf{y} . In particular, no semantic generation is required, and the reconstruction is predominantly governed by the likelihood.

Examples: Denoising, deconvolution with known kernel, low-dose (full-angle) CT, PET, electrical impedance tomography with full boundary measurements, ...

Type II (Identifiable) Advancing along the spectrum, we have problems where \mathbf{A} has a non-trivial nullspace $N(\mathbf{A})$, but $N(\mathbf{A})$ is incoherent with the image manifold \mathcal{M} , meaning that $\text{diam}(\mathcal{S}_{\mathbf{y}}^{\delta})$ remains small. In this regime, the data \mathbf{y} together with prior information *effectively* determine a unique reconstruction (up to small perturbations). Here, we require a *selection operator* that extracts the unique realistic reconstruction $\hat{\mathbf{x}}$ from $\mathcal{X}_{\mathbf{y}}^{\delta}$. Such selection operators are studied by Benning and Burger [2018]. Identifiability is also closely related to the compressed sensing [Donoho, 2006], where incoherence conditions such as the restricted isometry property guarantee identifiability.

Examples: Random inpainting, (mild) super-resolution, sparse-angle CT, compressed sensing MRI (undersampled k-space), single-pixel imaging with random masks, ...

Type III (Non-Identifiable) At the other end of the spectrum, the inverse problem has multiple realistic reconstructions in \mathcal{M} that are consistent with the data \mathbf{y} . Then, $\mathcal{S}_{\mathbf{y}}^{\delta}$ contains multiple well-separated reconstructions and its diameter $\text{diam}(\mathcal{S}_{\mathbf{y}}^{\delta})$ remains large even as $\delta \rightarrow 0$. In this case, the reconstruction method must *generate* plausible content in $N(\mathbf{A})$ based on the encoded knowledge about \mathcal{M} . This type is less dominant in scientific or medical imaging since experiments are usually designed such that sufficient information is captured (potentially with a very weak signal).

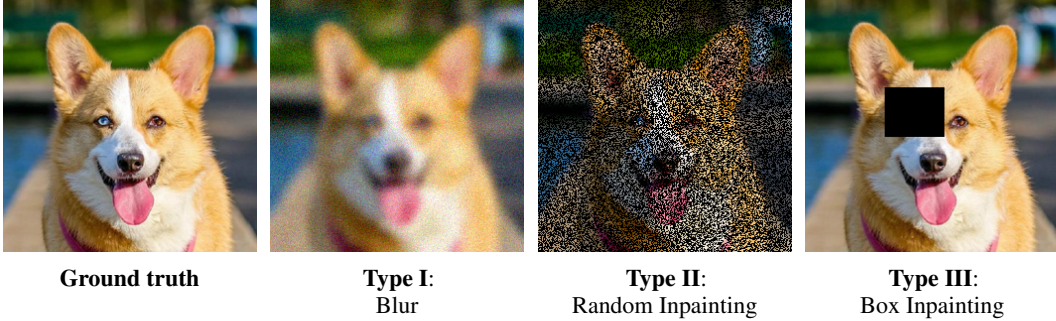


Figure 1: Illustration of the three types. Type I (Gaussian blur) is injective but severely ill-conditioned. Fine details are suppressed, while global semantic structure remains visible. Type II (60% random inpainting) induces a large, spatially dispersed nullspace. Despite substantial information loss, the semantics remain visible. Type III (box inpainting) has a localised nullspace. Part of the semantic content is lost, e.g., the color of the dog’s left eye.

Examples: Box-inpainting, image editing, image colorization, extreme image super-resolution, single-image 3D reconstruction, limited angle CT, ...

Role of noise Measurement noise interplays with our classification in a non-uniform way. For Type I, noise is the *primary* source of difficulty, i.e., reducing the misfit δ directly shrinks the set of possible solution \mathcal{S}_y^δ and diminishes the importance of prior information. In Type II, noise enlarges an otherwise small admissible set; consequently, decreasing δ restores near-identifiability and reduces reliance on prior information. By contrast, in Type III, the set of admissible solutions \mathcal{S}_y^δ remains large regardless of δ due to the inherent ambiguity of the forward operator \mathbf{A} . As a result, injecting prior knowledge remains crucial for successful reconstruction across all δ .

This is consistent with classical results in Bayesian statistics [Van der Vaart, 2000]. As data becomes more informative, the posterior distribution concentrates around the likelihood and the prior distribution becomes less influential. Conversely, as the problem shifts towards Type III, the posterior distribution remains heavily shaped by the prior distribution.

3 Overview on Reconstruction Methods

In the following, we briefly review the reconstruction methods under comparison. We focus on learned methods that depend only on the dataset and not the operator \mathbf{A} . At evaluation time, these require tuning of only a small number of hyperparameters. We exclude task-specific approaches, such as post-processing or unrolled methods, which often achieve state-of-the-art performance when the exact evaluation task is known already during training.

3.1 Variational Reconstruction with Learned Regularizers

Many reconstruction methods arise from minimizing the variational problem

$$\hat{\mathbf{x}} = \operatorname{argmin}_{\mathbf{x} \in \mathbb{R}^N} \frac{1}{2} \|\mathbf{Ax} - \mathbf{y}\|^2 + \lambda \mathcal{R}(\mathbf{x}), \quad (2)$$

where the regularizer \mathcal{R} captures prior information and $\lambda > 0$ is balancing the data fit. From a Bayesian perspective, \mathcal{R} is related to the prior distribution p by $\mathcal{R}(\mathbf{x}) = -\log(p(\mathbf{x}))$. Classic choices of \mathcal{R} like total variation [Rudin et al., 1992], wavelet priors [Daubechies, 1988] or compressed sensing models [Candès and Wakin, 2008] are usually not competitive with deep-learning approaches. Thus, there is growing interest in learning \mathcal{R} from data, see Habring and Holler [2024], Hertrich et al. [2026] for an overview. In our comparison, we consider two instances. First, the weakly convex ridge regularizer (WCRR) [Goujon et al., 2024] promises fast training times and good generalization properties, albeit with limited expressivity. Second, the least squares residual (LSR) [Hurault et al., 2022, Zou et al., 2023] is of the form $\mathcal{R}(\mathbf{x}) = \|\mathbf{x} - D(\mathbf{x})\|^2$, where D is a DRUNet [Zhang et al., 2022]. It provides more flexibility but requires significantly longer training. We train both regularizers by a bilevel approach [Ji et al., 2021] on a denoising problem using the codebase by Hertrich et al.

[2026]. Such learned regularizers are strongly connected to plug-and-play approaches [Hurault, 2023, Kamilov et al., 2023, Venkatakrishnan et al., 2013], which model the regularizer \mathcal{R} implicitly through denoisers that are typically trained on broad, task-agnostic datasets. In line with this framework, we additionally consider a (still explicit) plug-and-play variant of LSR (we refer to it as PnP-LSR), which is trained on the BSDS500 dataset [Arbeláez et al., 2011] consisting of natural images.

3.2 Diffusion-Based Inverse Problem Solvers

Diffusion models approximate the prior distribution $p(\mathbf{x})$ by reversing a gradual noising process. The forward process corrupts a clean sample \mathbf{x}_0 into a noisy version \mathbf{x}_t at time step t according to

$$\mathbf{x}_t = \sqrt{\bar{\alpha}_t} \mathbf{x}_0 + \sqrt{1 - \bar{\alpha}_t} \boldsymbol{\epsilon}, \quad \boldsymbol{\epsilon} \sim \mathcal{N}(\mathbf{0}, \mathbf{I}),$$

where $\bar{\alpha}_t$ defines the noise schedule. Sampling from the prior is achieved by the reverse-time dynamics

$$\mathbf{x}_{t-1} = \frac{1}{\sqrt{\alpha_t}} \left(\mathbf{x}_t - \frac{\beta_t}{\sqrt{1 - \bar{\alpha}_t}} \boldsymbol{\epsilon}_\theta(\mathbf{x}_t, t) \right) + \sqrt{\beta_t} \boldsymbol{\epsilon}_t, \quad \boldsymbol{\epsilon}_t \sim \mathcal{N}(\mathbf{0}, \mathbf{I}), \quad (3)$$

where the neural network $\boldsymbol{\epsilon}_\theta(\mathbf{x}_t, t)$ is trained to predict the noise component relating \mathbf{x}_t and \mathbf{x}_0 . By adapting the process (3) to enforce consistency with corrupted data $\mathbf{y} = \mathbf{A}\mathbf{x} + \boldsymbol{\eta}$, diffusion models can serve as powerful inverse problem solvers. Below, we compare four representative instances, and refer to the recent reviews by Daras et al. [2024], Luo et al. [2025] for an overview. Detailed derivations and full algorithms can be found in Appendix D.

Diffusion Posterior Sampling (DPS) Guidance-based methods, such as DPS [Chung et al., 2023], modify the unconditional reverse diffusion process (3) to sample from the posterior $p(\mathbf{x}_t | \mathbf{y})$. They achieve this by adding a data-consistency gradient, which pulls the process (3) towards data-consistent samples. Although originally designed for posterior sampling rather than point estimation, we include DPS since many works treat single-sample outputs as a (stochastic) reconstruction method.

Plug-and-Play Diffusion Methods The plug-and-play framework leverages diffusion models as highly expressive denoisers within classical optimization schemes [Li et al., 2024, Wu et al., 2024, Xu and Chi, 2024]. The selected representative method DiffPIR [Zhu et al., 2023] alternates between three steps: denoising the current estimate with the diffusion model, computing a data-consistency update, and subsequently re-injecting noise. The latter ensures that intermediate reconstructions remain on the correct diffusion manifold for the next time step.

Variational Reconstruction Rather than adapting the diffusion trajectory, variational methods like RED-diff [Mardani et al., 2024] construct an explicit regularization functional \mathcal{R} for (2) based on the diffusion model. Building on the Regularization by Denoising (RED) framework [Romano et al., 2017], RED-diff penalizes images that the diffusion model fails to denoise effectively. The objective is minimized using standard gradient-based optimizers (e.g., Adam [Kingma and Ba, 2015]) and by annealing the noise level across iterations.

Latent Space Optimization Latent space optimization methods such as DMPlug [Wang et al., 2024] or D-Flow [Ben-Hamu et al., 2024] utilize deterministic diffusion samplers (such as DDIM [Song et al., 2021]) as differentiable image generators. Then, to minimize the data-consistency loss, they optimize directly over the initial latent code \mathbf{z} . As this is susceptible to overfitting the measurement noise, they rely on heuristics, e.g., early stopping or additional regularization [Ben-Hamu et al., 2024]. As a representative instance, we compare against DMPlug with early stopping.

3.3 PnP-Flow

Flow matching is closely related to diffusion models but learns a deterministic velocity field instead of the score network $\boldsymbol{\epsilon}_\theta(\mathbf{x}_t, t)$. Martin et al. [2025] propose a PnP scheme by reinterpreting the velocity field as a denoiser. Then, similarly to DiffPIR, it alternates denoising steps, data-consistency updates and re-injection of noise, see Appendix E for details. In our experiments, PnP-flow as proposed by Martin et al. [2025] becomes unstable at low noise levels. Thus, in line with other classical PnP approaches, we replace the data-fidelity gradient step by a proximal step.

4 Experiments

Next, we want to benchmark how well the methods from Section 3 meet the desirable properties of a reconstruction method. Our experiments target the following settings:

1. **In-distribution:** We compare the reconstruction performance in an idealized setting where training and test data are independent samples from the same distribution.
2. **Out-of-distribution:** We use different datasets for training and testing. By varying the degree of the mismatch, we check how well the methods generalize to OOD data.
3. **Operator and Noise Model Mismatch:** (Appendix B.5): We use slightly different forward operators and noise models for the training data generation and testing. This assesses the stability regarding (unavoidable) modeling errors that occur in practice.

Further, we investigate in Appendix B the stability regarding different noise realizations (Appendix B.2), the behavior in over- and underregularized settings (Appendix B.3), and a comparison with FlowDPS which guides a large text-to-image latent diffusion model (Stable Diffusion 3.0, Esser et al., 2024; Appendix B.4).

Scientific Imaging Setup As a prototypical scientific imaging task, we consider parallel-beam computed tomography (CT) with a varying number of equi-spaced angles. This is implemented as part of the `deepinv` library [Tachella et al., 2025] with the `Astra` backend [Van Aarle et al., 2015]. We evaluate all models on the `Walnut` dataset [Der Sarkissian et al., 2019]. While this setup does not reflect any clinical application, it allows precise control over the information content of the forward operator \mathbf{A} (via the number of angles) and the noise level, making it well suited for analyzing the desirable properties of reconstruction methods. The full experimental settings are provided in Appendix F. Further, in Appendix A, we include a similar study on natural images.

Competing Methods and Evaluation Metrics For all methods, we tune the hyperparameters with a grid search on a validation set. We provide a detailed description and a table with the found hyperparameters in Appendix F. To compare all results, we use the following evaluation metrics.

1. **Peak Signal-to-Noise Ratio (PSNR):** A popular and simple metric is PSNR, which for images with dynamic range $[0, 1]$ is defined as $\text{PSNR}(\mathbf{x}, \mathbf{x}_{\text{true}}) = -10 \log(\|\mathbf{x} - \mathbf{x}_{\text{true}}\|^2 / \#\text{pixels})$.
2. **Structural Similarity (SSIM):** The SSIM [Wang et al., 2004] is a widely used metric that compares structural patterns like luminance and contrast locally for two images.
3. **Learned Perceptual Metrics (LPIPS):** The more recent metric LPIPS [Zhang et al., 2018] compares deep features learned by a classification network.
4. **Data-Consistency:** The (relative) data-consistency for a reconstruction \mathbf{x} and data \mathbf{y} is defined as $\text{DC}(\mathbf{x}, \mathbf{y}) = \|\mathbf{A}\mathbf{x} - \mathbf{y}\|^2 / \mathbb{E}[\|\mathbf{A}\mathbf{x}_{\text{true}} - \mathbf{y}\|^2]$. Values significantly larger than one indicate that the reconstruction \mathbf{x} does not remain faithful to the data \mathbf{y} and instabilities might occur.

Further, we provide a comparison of the computation times of all approaches in Figure 4.

4.1 In-Distribution Performance

Table 1 shows the in-distribution performance of all methods for parallel-beam CT with 16, 32, 64 and 128 angles, where the latter represent different levels of information loss. The associated simulated data is corrupted by additive Gaussian noise with $\sigma_n = 0.01$. For the impact of using different noise realizations, see Table 5 of Appendix B.2. We observe that the learned regularizer LSR always achieves one of the highest PSNR values, while diffusion priors (DiffPIR, RED-diff and DPS) tend to generate the highest SSIM and LPIPS scores. The PnP-flow performs well in both metrics. For 16 and 32 angles (low information content), all generative priors (including PnP-flow) achieve a drastically lower PSNR value than the LSR, while some of them (PnP-flow and DiffPIR) achieve competitive SSIM and LPIPS values. The qualitative comparison of LSR, DiffPIR and PnP-flow in Figure 2 (see Figure 11 in Appendix B for the other methods) suggests that this is due to data-consistent hallucinations (namely DC remains below one) of the diffusion approaches. These are particularly pronounced for the 8 and 16 angle settings, which are of Type III. Further, we note that DMPlug already fails to produce data-consistent reconstructions in this setting and requires excessive computational effort; we therefore exclude it from subsequent experiments.

In Figure 3 (see Table 3 in Appendix B for the remaining metrics), we showcase the behavior of the PSNR as the noise level σ_n approaches zero. Specifically, we consider the setting with 128 angles and $\sigma_n \in \{0.005, 0.002, 0.001, 0.0\}$. Since \mathbf{A} is highly informative, a *convergent regularization*

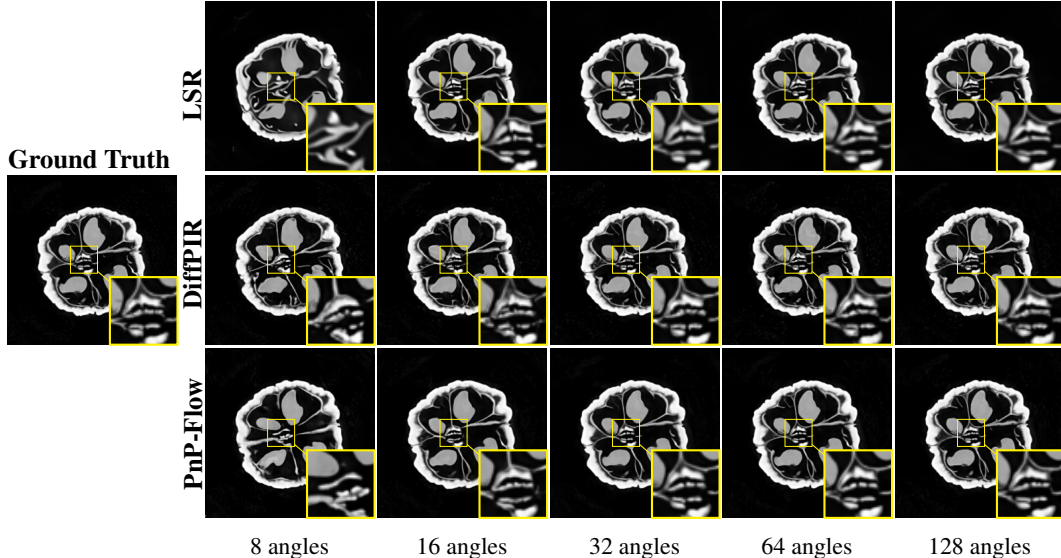


Figure 2: Reconstruction of a walnut slice for various number of angles. While being of Type I/II for 128 angles, the task is very hard (Type III) for only 8 angles. This is underlined by the hallucinations (artificial structures) that are visible in the magnified square. See Figure 11 for the remaining methods.

Table 1: CT reconstruction metrics with additive Gaussian noise ($\sigma_n = 0.01$). Best values are in bold, second-best are underlined. The hyperparameters of each method are tuned to maximize validation PSNR. Table 5 reports the impact of different noise realizations.

Method	Walnut \rightarrow Walnut (in-distribution)															
	Sparse View (16 angles)				Sparse View (32 angles)				Sparse View (64 angles)				Sparse View (128 angles)			
	PSNR \uparrow	SSIM \uparrow	LPIPS \downarrow	DC	PSNR \uparrow	SSIM \uparrow	LPIPS \downarrow	DC	PSNR \uparrow	SSIM \uparrow	LPIPS \downarrow	DC	PSNR \uparrow	SSIM \uparrow	LPIPS \downarrow	DC
FBP	11.13	0.164	0.624	336.3	15.45	0.237	0.587	25.51	18.65	0.296	0.620	1.805	19.92	0.320	0.663	0.474
TV	23.24	0.816	0.155	0.611	26.66	0.884	0.110	0.721	28.20	0.902	0.091	0.821	28.51	0.901	0.088	0.898
PnP-LSR	22.48	0.674	0.290	3.256	29.18	0.914	0.091	0.901	30.74	0.897	0.072	0.813	30.87	0.890	0.067	0.890
WCRR	24.97	0.872	0.116	0.877	29.07	0.901	0.067	0.719	30.42	0.896	0.056	0.798	30.59	0.886	0.053	0.879
LSR	29.60	<u>0.900</u>	0.041	0.600	31.86	0.881	0.042	0.920	<u>32.66</u>	0.884	<u>0.037</u>	0.944	<u>32.81</u>	0.885	0.035	0.969
DiffPIR	<u>27.71</u>	<u>0.900</u>	0.032	0.629	30.90	<u>0.929</u>	0.020	0.795	31.71	<u>0.928</u>	0.020	0.859	31.85	0.939	0.015	0.957
DMPPlug	19.71	0.629	0.234	35.55	19.66	0.619	0.252	23.43	19.53	0.606	0.259	13.32	19.66	0.626	0.239	6.427
DPS	22.84	0.834	0.104	3.656	25.75	0.740	0.101	5.372	26.91	0.781	0.087	2.596	27.61	0.959	0.073	1.299
RED-diff	27.07	0.826	0.068	0.341	29.61	0.827	0.062	0.531	30.29	0.844	0.056	0.760	27.51	0.865	0.069	1.001
PnP-Flow	27.56	0.913	<u>0.039</u>	0.715	<u>31.24</u>	0.944	<u>0.027</u>	0.841	32.81	0.950	0.020	0.884	33.11	<u>0.950</u>	<u>0.018</u>	0.932

method should converge to the ground truth as $\sigma_n \rightarrow 0$. We observe that this is true for the variational methods (TV, WCRR and LSR). Among the generative priors, only the PnP-flow fully meets this requirement. While DiffPIR still approaches the ground truth, RED-diff already struggles for small noise levels. DPS fails to produce more accurate results as $\sigma_n \rightarrow 0$. Thus, the data consistency term DC explodes. We discuss this behavior in Section 5.

4.2 Out-of-Distribution Data

Next, we benchmark the stability of all methods towards OOD images, which frequently occur in practice. Moreover, according to the typical “plug-and-play” paradigm, it should suffice to train on a rich enough dataset, which might be different from the evaluation setting. To analyze the stability, we alter the training dataset, while maintaining the 128 angle evaluation setting from Section 4.1. In particular, we retrain all models on the following datasets (see example images in Figure 10).

1. AAPM [McCullough et al., 2017], which contains images acquired with CT, but containing human organs rather than walnuts. Thus, the image characteristics are very different.
2. Ellipses [Barbano et al., 2022] is a synthetic dataset, where each image is populated with up to 70 ellipses. Indeed, piecewise constant images are a common prior in the CT domain.

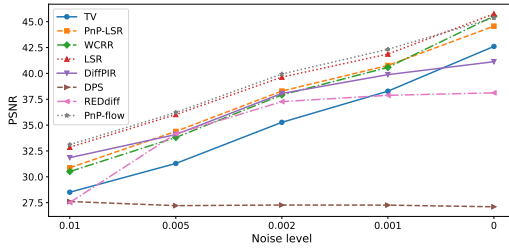


Figure 3: Reconstruction PSNR as $\sigma_n \rightarrow 0$. Convergent methods should approach high values.

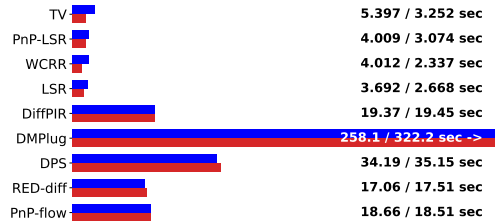


Figure 4: Average computation time per sample for 32 (blue) and 128 angles (red) from Table 1.

- CelebA-HQ [Karras et al., 2018] is a diverse dataset showing human faces of celebrities. Note that this model is trained on RGB images. During inference, we copy the single-channel CT images into three channels and average the predicted outputs, see Appendix F.4 for a description.

The results are visualized in Figure 5 (see Table 4 in Appendix B for the remaining metrics). We find that generative priors significantly degrade compared to the in-distribution scenario, especially in terms of LPIPS. Specifically, DPS, RED-diff and PnP-flow consistently produce worse results than the simple (non-learned) TV baseline. By contrast, the learned regularizers WCRR and LSR are considerably more robust: Although LSR still shows a drop in performance when trained on Ellipses, it performs reasonably well when trained on AAPM or CelebA-HQ, but still worse than PnP-LSR (which is trained on BSDS500). Among all reconstruction approaches considered, WCRR is the only one that consistently outperforms TV in terms of PSNR and matches it in terms of LPIPS. DiffPIR fails to deliver meaningful reconstructions when trained on AAPM or Ellipses; when trained on CelebA-HQ, it does surpass TV but remains inferior to LSR and PnP-LSR. In Appendix B.4, we find that also using a large text-to-image diffusion model as prior does not improve the results. A visual comparison of LSR and PnP-flow is given in Figure 6 and a complete comparison is given in Figure 12 of Appendix B. For the models trained on Ellipses, we observe a clear bias towards piecewise constant reconstructions. In contrast, CelebA-HQ leads to a stronger smoothing.

5 Discussion and Conclusion

In the following, we formulate three key takeaways from the numerical experiments. Further aspects like the computation time, the relevance of the problem type, stability towards the forward model, and insights from our experiments on natural images are included in Appendix C.

Data Handling (Explicit vs Implicit) Among the generative priors, DPS and RED-diff achieve data consistency by explicit gradient steps of the data term. In contrast, DiffPIR and PnP-flow (adapted as in Appendix E) use an implicit gradient step. Across all experiments, DiffPIR and PnP-flow significantly outperform DPS and RED-diff. Moreover, DPS and RED-diff do not pass the convergent regularization test from Figure 3. Tracking the data consistency in Tables 1 and 3 reveals the insufficient handling of the data term as a potential reason. For variational methods, this is no issue as the objective is minimized with a convergent scheme.

Takeaway: In scientific imaging, the correct handling of the data term is crucial. In particular, methods with implicit gradient steps (DiffPIR, implicit PnP-flow) or variational methods like LSR are preferable over diffusion methods with explicit gradient steps (DPS, RED-diff).

Stability (Expressiveness vs Generalization) Usually, the desirable properties from Section 1 compete against each other, see also Genzel et al. [2022], Gottschling et al. [2025]. We examine this through the lens of sensitivity to OOD settings. While (PnP-)LSR improves upon classical baselines like TV even when trained on generic images, this robustness is not shared by the benchmarked diffusion methods. We hypothesize that this discrepancy is closely linked to model capacity. For instance, the lightweight WCRR (10k parameters) outperforms TV even when trained on the synthetic Ellipses dataset. Conversely, the LSR (4M parameters) exhibits a clear structural bias when trained on Ellipses (see Figure 6), yet yields significant improvements when trained on richer datasets like CelebA-HQ or BSDS500. Large-scale diffusion priors (80M parameters), however, tend to strictly

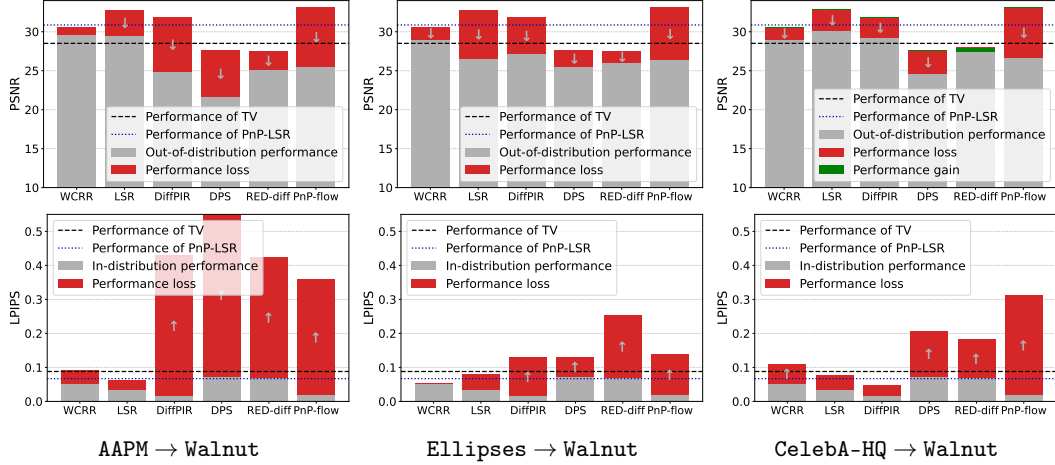


Figure 5: Train–test mismatch robustness for parallel-beam CT with 128 angles. The red portion of each bar indicates the performance loss incurred when using a training set different from Walnut. The dashed black line represents the performance of TV, which is independent of the training data.

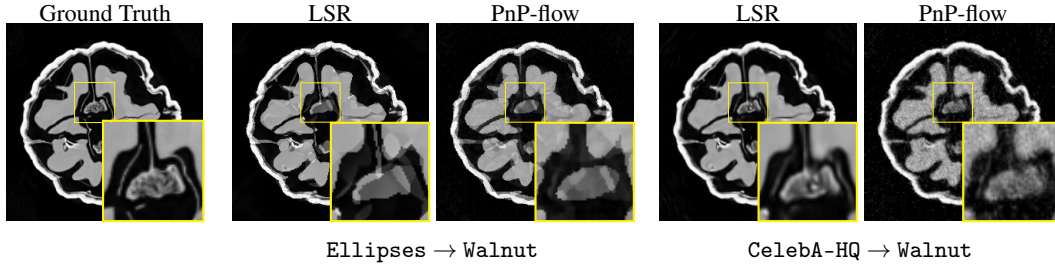


Figure 6: OOD reconstructions for LSR and PnP-flow in the 32-angle setting. The implicit bias induced by the training data varies substantially. Remaining methods are shown in Figure 12.

reproduce their training distribution, failing to generate meaningful reconstructions outside that regime. Furthermore, even when guiding Stable Diffusion 3.0 with Flow-DPS (Appendix B.4 and Table 6), performance remains inferior to both DiffPIR and PnP-LSR (both trained OOD).

Takeaway: When out-of-distribution test data is anticipated, smaller models exhibit substantially better generalization. In these scenarios, variational approaches such as LSR are preferable to generative priors. This situation arises in many scientific imaging applications.

Perception vs Distortion Across all experiments, generative priors demonstrate superior perceptual performance (LPIPS), whereas variational methods such as (PnP-)LSR yield better distortion-based metrics (PSNR, SSIM). We attribute this discrepancy to the handling of missing data. As illustrated in Figure 13, over-regularization with a generative prior in Type I or II problems leads to the hallucination of realistic-looking features. In contrast, variational priors like (PnP-)LSR tend to produce blurred reconstructions when faced with uncertainty. Figures 2, 9, and 11 confirm that this behavior persists in Type III problems involving missing measurement information. In scientific applications, visible blurring is generally preferred over convincing hallucinations, as the former is easily identified as a reconstruction failure, whereas the latter can lead to erroneous interpretations.

Takeaway: When information is missing, variational methods (LSR) tend to “wash out” the unknown regions, whereas generative priors (DiffPIR, DPS, and RED-diff) hallucinate realistic-looking structures. In the context of scientific and medical domain, the latter is more harmful.

Limitations Our study is restricted to a small collection of inverse problems and a limited number of reconstruction approaches. While we conjecture that similar conclusions can be drawn in many common setups, our experiments do not directly transfer to new scenarios. Similarly, while we use

standard architectures and model sizes, the results of our tests might change if significantly larger models and datasets are used. Even if we believe that our setup covers common scenarios, these computational restrictions limit the generality of our study. See Appendix C for more details.

Overall Conclusion / Opinion: While stability and faithfulness to the data remain crucial for solving inverse problems in scientific or medical settings, they remain widely underexplored. Benchmarks and papers considering image reconstruction methods should include some standard stability tests (similar to our tests in Section 4.1 and 4.2) and report the data consistency.

Acknowledgments and Disclosure of Funding

AD acknowledges support from the EPSRC (EP/V026259/1) and support from DESY (Hamburg, Germany), a member of the Helmholtz Association HGF. JH acknowledges funding by the Deutsche Forschungsgemeinschaft (DFG, German Research Foundation) with project no 530824055. SN acknowledges support from the DFG (grant SPP2298 - 543939932).

References

- Michael S Albergo and Eric Vanden-Eijnden. Building normalizing flows with stochastic interpolants. In *The 11th International Conference on Learning Representations*, 2023.
- Pablo Arbeláez, Michael Maire, Charless Fowlkes, and Jitendra Malik. Contour detection and hierarchical image segmentation. *IEEE Trans. Pattern Anal. Mach. Intell.*, 33(5):898–916, 2011.
- Simon Arridge, Peter Maass, Ozan Öktem, and Carola-Bibiane Schönlieb. Solving inverse problems using data-driven models. *Acta Numer.*, 28:1–174, 2019.
- Riccardo Barbano, Johannes Leuschner, Maximilian Schmidt, Alexander Denker, Andreas Hauptmann, Peter Maass, and Bangti Jin. An educated warm start for deep image prior-based micro CT reconstruction. *IEEE Trans. Comput. Imaging*, 8:1210–1222, 2022.
- Heli Ben-Hamu, Omri Puny, Itai Gat, Brian Karrer, Uriel Singer, and Yaron Lipman. D-flow: Differentiating through flows for controlled generation. In *Proceedings of the 41st International Conference on Machine Learning*, pages 3462–3483. PMLR, 2024.
- Martin Benning and Martin Burger. Modern regularization methods for inverse problems. *Acta Numer.*, 27:1–111, 2018.
- Ashish Bora, Ajil Jalal, Eric Price, and Alexandros G Dimakis. Compressed sensing using generative models. In *Proceedings of the 34th International Conference on Machine Learning*, pages 537–546. PMLR, 2017.
- Emmanuel J Candès and Michael B Wakin. An introduction to compressive sampling. *IEEE Signal Process. Mag.*, 25(2):21–30, 2008.
- Hamadi Chihoui, Abdelhak Lemkhenter, and Paolo Favaro. Blind image restoration via fast diffusion inversion. In *Advances in Neural Information Processing Systems*, volume 37, pages 34513–34532. Curran Associates, Inc., 2024.
- Yunjey Choi, Youngjung Uh, Jaejun Yoo, and Jung-Woo Ha. Stargan v2: Diverse image synthesis for multiple domains. In *Proceedings of the IEEE/CVF International Conference on Computer Vision*, pages 8188–8197, 2020.
- Hyungjin Chung, Jeongsol Kim, Michael Thompson Mccann, Marc Louis Klasky, and Jong Chul Ye. Diffusion posterior sampling for general noisy inverse problems. In *The 11th International Conference on Learning Representations*, 2023.
- Laurent Condat. A primal-dual splitting method for convex optimization involving Lipschitzian, proximable and linear composite terms. *J. Optim. Theory Appl.*, 158(2):460–479, 2013.
- Evan Scope Crafts and Umberto Villa. Benchmarking diffusion annealing-based Bayesian inverse problem solvers. *IEEE Open J. Signal Process.*, 6:975–991, 2025.

- Giannis Daras, Hyungjin Chung, Chieh-Hsin Lai, Yuki Mitsufuji, Jong Chul Ye, Peyman Milanfar, Alexandros G Dimakis, and Mauricio Delbracio. A survey on diffusion models for inverse problems. *arXiv preprint arXiv:2410.00083*, 2024.
- Ingrid Daubechies. Orthonormal bases of compactly supported wavelets. *Commun. Pur. Appl. Math.*, 41(7):909–996, 1988.
- Alexander Denker, Francisco Vargas, Shreyas Padhy, Kieran Didi, Simon Mathis, Vincent Dutoir, Riccardo Barbano, Emile Mathieu, Urszula J Komorowska, and Pietro Lio. Deft: Efficient fine-tuning of diffusion models by learning the generalised h -transform. In *Advances in Neural Information Processing Systems*, volume 37, pages 19636–19682. Curran Associates, Inc., 2024.
- Alexander Denker, Moshe Eliasof, Zeljko Kereta, and Carola-Bibiane Schönlieb. Trajectory stitching for solving inverse problems with flow-based models. *arXiv preprint arXiv:2602.08538*, 2026.
- Henri Der Sarkissian, Felix Lucka, Maureen Van Eijnatten, Giulia Colacicco, Sophia Bethany Coban, and Kees Joost Batenburg. A cone-beam X-ray computed tomography data collection designed for machine learning. *Sci. Data*, 6(1):215, 2019.
- David L Donoho. Compressed sensing. *IEEE Trans. Inform. Theory*, 52(4):1289–1306, 2006.
- Joseph L Doob. Application of the theory of martingales. *Le Calcul des Probabilités et ses Applications*, 13:23–27, 1949.
- Hongkun Dou, Zeyu Li, Jinyang Du, Lijun Yang, Wen Yao, and Yue Deng. Hybrid regularization improves diffusion-based inverse problem solving. In *The 13th International Conference on Learning Representations*, 2025.
- Margaret A G Duff, Neill D F Campbell, and Matthias J Ehrhardt. Regularising inverse problems with generative machine learning models. *J. Math. Imaging and Vis.*, 66(1):37–56, 2024.
- Andrea Ebner and Markus Haltmeier. Plug-and-play image reconstruction is a convergent regularization method. *IEEE Trans. Image Process.*, 33:1476–1486, 2024.
- Heinz W. Engl, Martin Hanke, and Andreas Neubauer. *Regularization of Inverse Problems*. Kluwer Academic Publishers Group, Dordrecht, 1996.
- Julius Erbach, Dominik Narnhofer, Andreas Robert Dombos, Bernt Schiele, Jan Eric Lenssen, and Konrad Schindler. Solving inverse problems with FLAIR. In *Advances in Neural Information Processing Systems*, volume 38. Curran Associates, Inc., 2026.
- Patrick Esser, Sumith Kulal, Andreas Blattmann, Rahim Entezari, Jonas Müller, Harry Saini, Yam Levi, Dominik Lorenz, Axel Sauer, Frederic Boesel, et al. Scaling rectified flow transformers for high-resolution image synthesis. In *Proceedings of the 41st International Conference on Machine Learning*, pages 12606–12633. PMLR, 2024.
- Martin Genzel, Jan Macdonald, and Maximilian März. Solving inverse problems with deep neural networks—robustness included? *IEEE Trans. Pattern Anal. Mach. Intell.*, 45(1):1119–1134, 2022.
- Nina M. Gottschling, Vegard Antun, Anders C. Hansen, and Ben Adcock. The troublesome kernel: On hallucinations, no free lunches, and the accuracy-stability tradeoff in inverse problems. *SIAM Rev.*, 67(1):73–104, 2025.
- Alexis Goujon, Sebastian Neumayer, and Michael Unser. Learning weakly convex regularizers for convergent image-reconstruction algorithms. *SIAM J. Imaging Sci.*, 17(1):91–115, 2024.
- Andreas Habring and Martin Holler. Neural-network-based regularization methods for inverse problems in imaging. *GAMM-Mitteilungen*, 47(4):e202470004, 2024.
- Andreas Hauptmann, Subhadip Mukherjee, Carola-Bibiane Schönlieb, and Ferdia Sherry. Convergent regularization in inverse problems and linear plug-and-play denoisers. *Found. Comput. Math.*, 25(4):1087–1120, 2025.

- Johannes Hertrich, Hok Shing Wong, Alexander Denker, Stanislas Ducotterd, Zhenghan Fang, Markus Haltmeier, Željko Kereta, Erich Kobler, Oscar Leong, Mohammad Sadegh Salehi, Carola-Bibiane Schönlieb, Johannes Schwab, Zakhar Shumaylov, Jeremias Sulam, German Shâma Wache, Martin Zach, Yasi Zhang, Matthias J. Ehrhardt, and Sebastian Neumayer. Learning regularization functionals for inverse problems: a comparative study. *Handbook of Numerical Analysis*. Elsevier, 2026. doi: <https://doi.org/10.1016/bs.hna.2026.04.001>.
- Jonathan Ho, Ajay Jain, and Pieter Abbeel. Denoising diffusion probabilistic models. In *Advances in Neural Information Processing Systems*, volume 33, pages 6840–6851. Curran Associates, Inc., 2020.
- Samuel Hurault. *Convergent plug-and-play methods for image inverse problems with explicit and nonconvex deep regularization*. PhD thesis, Université de Bordeaux, 2023.
- Samuel Hurault, Arthur Leclaire, and Nicolas Papadakis. Gradient step denoiser for convergent Plug-and-Play. In *The 10th International Conference on Learning Representations*, 2022.
- Kaiyi Ji, Junjie Yang, and Yingbin Liang. Bilevel optimization: Convergence analysis and enhanced design. In *Proceedings of the 38th International Conference on Machine Learning*, pages 4882–4892. PMLR, 2021.
- Jing Jia, Wei Yuan, Sifan Liu, Liyue Shen, and Guanyang Wang. Weak diffusion priors can still achieve strong inverse-problem performance. *arXiv preprint arXiv:2601.22443*, 2026.
- Ulugbek S Kamilov, Charles A Bouman, Gregory T Buzzard, and Brendt Wohlberg. Plug-and-play methods for integrating physical and learned models in computational imaging: Theory, algorithms, and applications. *IEEE Signal Process. Mag.*, 40(1):85–97, 2023.
- Tero Karras, Timo Aila, Samuli Laine, and Jaakko Lehtinen. Progressive growing of GANs for improved quality, stability, and variation. In *The 6th International Conference on Learning Representations*, 2018.
- Tero Karras, Samuli Laine, and Timo Aila. A style-based generator architecture for generative adversarial networks. In *Proceedings of the IEEE/CVF Conference on Computer Vision and Pattern Recognition*, pages 4401–4410, 2019.
- Bahjat Kawar, Michael Elad, Stefano Ermon, and Jiaming Song. Denoising diffusion restoration models. In *Advances in Neural Information Processing Systems*, volume 35, pages 23593–23606. Curran Associates, Inc., 2022.
- Jeongsol Kim, Bryan Sangwoo Kim, and Jong Chul Ye. Flowdps: Flow-driven posterior sampling for inverse problems. In *Proceedings of the IEEE/CVF International Conference on Computer Vision*, pages 12328–12337, 2025.
- Diederik P Kingma and Jimmy Ba. Adam: A method for stochastic optimization. In *The 3rd International Conference on Learning Representations*, 2015.
- Maximilian B Kiss, Ander Biguri, Zakhar Shumaylov, Ferdia Sherry, K Joost Batenburg, Carola-Bibiane Schönlieb, and Felix Lucka. Benchmarking learned algorithms for computed tomography image reconstruction tasks. *Appl. Math. Mod. Challenges*, 3:1–43, 2025.
- Black Forest Labs. FLUX.2: Frontier Visual Intelligence. <https://bf1.ai/blog/flux-2>, 2025.
- Anat Levin, Yair Weiss, Fredo Durand, and William T Freeman. Understanding and evaluating blind deconvolution algorithms. In *Proceedings of the IEEE Conference on Computer Vision and Pattern Recognition*, pages 1964–1971, 2009.
- Huan Li and Zhouchen Lin. Accelerated proximal gradient methods for nonconvex programming. In *Advances in Neural Information Processing Systems 28*, pages 379–387. Curran Associates, Inc., 2015.
- Xiang Li, Soo Min Kwon, Shijun Liang, Ismail R Alkhouri, Saiprasad Ravishankar, and Qing Qu. Decoupled data consistency with diffusion purification for image restoration. *arXiv preprint arXiv:2403.06054*, 2024.

- Yaron Lipman, Ricky T. Q. Chen, Heli Ben-Hamu, Maximilian Nickel, and Matthew Le. Flow matching for generative modeling. In *The 11th International Conference on Learning Representations*, 2023.
- Yaron Lipman, Marton Havasi, Peter Holderrieth, Neta Shaul, Matt Le, Brian Karrer, Ricky TQ Chen, David Lopez-Paz, Heli Ben-Hamu, and Itai Gat. Flow matching guide and code. *arXiv preprint arXiv:2412.06264*, 2024.
- Xingchao Liu, Chengyue Gong, and Qiang Liu. Flow straight and fast: Learning to generate and transfer data with rectified flow. In *The 11th International Conference on Learning Representations*, 2023.
- Ziwei Liu, Ping Luo, Xiaogang Wang, and Xiaoou Tang. Deep learning face attributes in the wild. In *Proceedings of the IEEE International Conference on Computer Vision*, pages 3730–3738, 2015.
- Ziwei Luo, Fredrik Gustafsson, Zheng Zhao, Jens Sjölund, and Thomas Schön. Taming diffusion models for image restoration: a review. *Philos. Trans. Roy. Soc. A*, 383(2299), 2025.
- Morteza Mardani, Jiaming Song, Jan Kautz, and Arash Vahdat. A variational perspective on solving inverse problems with diffusion models. In *The 12th International Conference on Learning Representations*, 2024.
- Ségolène Tiffany Martin, Anne Gagneux, Paul Hagemann, and Gabriele Steidl. PnP-Flow: Plug-and-play image restoration with flow matching. In *The 13th International Conference on Learning Representations*, 2025.
- Cynthia H McCollough, Adam C Bartley, Rickey E Carter, Baiyu Chen, Tammy A Drees, Phillip Edwards, David R Holmes III, Alice E Huang, Farhana Khan, Shuai Leng, et al. Low-dose CT for the detection and classification of metastatic liver lesions: results of the 2016 low dose CT grand challenge. *Med. Phys.*, 44(10):e339–e352, 2017.
- Sebastian Neumayer and Fabian Altekrieger. Stability of data-dependent ridge-regularization for inverse problems. *Inverse Probl.*, 41(6):e065006, 2025.
- Gregory Ongie, Ajil Jalal, Christopher A. Metzler, Richard G. Baraniuk, Alexandros G. Dimakis, and Rebecca Willett. Deep learning techniques for inverse problems in imaging. *IEEE Trans. Inf. Theory*, 1(1):39–56, 2020.
- Mehrsa Pourya, Bassam El Rawas, and Michael Unser. Flower: A flow-matching solver for inverse problems. In *The Fourteenth International Conference on Learning Representations*, 2026.
- Xiaoyu Qiu, Taewon Yang, Zhanhao Liu, Guanyang Wang, and Liyue Shen. Benchmarking uncertainty quantification of plug-and-play diffusion priors for inverse problems solving. *arXiv preprint arXiv:2602.04189*, 2026.
- Yaniv Romano, Michael Elad, and Peyman Milanfar. The little engine that could: Regularization by denoising (RED). *SIAM J. Imaging Sci.*, 10(4):1804–1844, 2017.
- Leonid I Rudin, Stanley Osher, and Emad Fatemi. Nonlinear total variation based noise removal algorithms. *Phys. D*, 60(1-4):259–268, 1992.
- Jiayang Shi, Daniel Pelt, and Joost Batenburg. DM4CT: Benchmarking diffusion models for computed tomography reconstruction. In *The 14th International Conference on Learning Representations*, 2026.
- Imraj RD Singh, Alexander Denker, Riccardo Barbano, Željko Kereta, Bangti Jin, Kris Thielemans, Peter Maass, and Simon Arridge. Score-based generative models for PET image reconstruction. *J. Mach. Learn. Biomed. Imaging*, 2:547–585, 2024.
- Jiaming Song, Chenlin Meng, and Stefano Ermon. Denoising diffusion implicit models. In *The 9th International Conference on Learning Representations*, 2021.
- Yang Song, Liyue Shen, Lei Xing, and Stefano Ermon. Solving inverse problems in medical imaging with score-based generative models. In *The 10th International Conference on Learning Representations*, 2022.

- Julián Tachella, Matthieu Terris, Samuel Hurault, Andrew Wang, Leo Davy, Jérémy Scanvic, Victor Sechaud, Romain Vo, Thomas Moreau, Thomas Davies, Dongdong Chen, Nils Laurent, Brayan Monroy, Jonathan Dong, Zhiyuan Hu, Minh-Hai Nguyen, Florian Sarron, Pierre Weiss, Paul Escande, Mathurin Massias, Thibaut Modrzyk, Brett Levac, Tobías I. Liaudat, Maxime Song, Johannes Hertrich, Sebastian Neumayer, and Georg Schramm. Deepinverse: A python package for solving imaging inverse problems with deep learning. *J. Open Source Softw.*, 10(115):8923, 2025.
- Matthieu Terris, Samuel Hurault, Maxime Song, and Julián Tachella. Reconstruct anything model a lightweight foundation model for computational imaging. In *The 14th International Conference on Learning Representations*, 2026.
- David YW Thong, Charlesquin Kemajou Mbakam, and Marcelo Pereyra. Do Bayesian imaging methods report trustworthy probabilities? *arXiv preprint arXiv:2405.08179*, 2024.
- Dmitry Ulyanov, Andrea Vedaldi, and Victor Lempitsky. Deep image prior. In *Proceedings of the IEEE Conference on Computer Vision and Pattern Recognition*, pages 9446–9454, 2018.
- Wim Van Aarle, Willem Jan Palenstijn, Jan De Beenhouwer, Thomas Altantzis, Sara Bals, K Joost Batenburg, and Jan Sijbers. The ASTRA toolbox: A platform for advanced algorithm development in electron tomography. *Ultramicroscopy*, 157:35–47, 2015.
- Aad W Van der Vaart. *Asymptotic Statistics*. Cambridge University Press, 2000.
- Singanallur V Venkatakrishnan, Charles A Bouman, and Brendt Wohlberg. Plug-and-play priors for model based reconstruction. In *IEEE Global Conference on Signal and Information Processing*, pages 945–948, 2013.
- Patrick von Platen, Suraj Patil, Anton Lozhkov, Pedro Cuenca, Nathan Lambert, Kashif Rasul, Mishig Davaadorj, Dhruv Nair, Sayak Paul, William Berman, Yiyi Xu, Steven Liu, and Thomas Wolf. Diffusers: State-of-the-art diffusion models. <https://github.com/huggingface/diffusers>, 2022.
- Hengkang Wang, Taihui Li, Zhong Zhuang, Tiancong Chen, Hengyue Liang, and Ju Sun. Early stopping for deep image prior. *arXiv preprint arXiv:2112.06074*, 2021.
- Hengkang Wang, Xu Zhang, Taihui Li, Yuxiang Wan, Tiancong Chen, and Ju Sun. Dmplug: A plug-in method for solving inverse problems with diffusion models. In *Advances in Neural Information Processing Systems*, volume 37, pages 117881–117916. Curran Associates, Inc., 2024.
- Yinhui Wang, Jiwen Yu, and Jian Zhang. Zero-shot image restoration using denoising diffusion null-space model. In *The 11th International Conference on Learning Representations*, 2023.
- Zhou Wang, Alan C Bovik, Hamid R Sheikh, and Eero P Simoncelli. Image quality assessment: from error visibility to structural similarity. *IEEE Trans. on Image Process.*, 13(4):600–612, 2004.
- George Webber and Andrew J Reader. Diffusion models for medical image reconstruction. *BJRl Artif. Intell.*, 1(1):ubae013, 2024.
- George Webber, Alexander Denker, Riccardo Barbano, and Andrew J Reader. Solving inverse problems with flow-based models via model predictive control. *arXiv preprint arXiv:2601.23231*, 2026.
- Zihui Wu, Yu Sun, Yifan Chen, Bingliang Zhang, Yisong Yue, and Katherine L Bouman. Principled probabilistic imaging using diffusion models as plug-and-play priors. In *Advances in Neural Information Processing Systems*, volume 37, pages 118389–118427. Curran Associates, Inc., 2024.
- Xingyu Xu and Yuejie Chi. Provably robust score-based diffusion posterior sampling for plug-and-play image reconstruction. In *Advances in Neural Information Processing Systems*, volume 37, pages 36148–36184. Curran Associates, Inc., 2024.
- Linfeng Ye, Shayan Mohajer Hamidi, Mert Pilanci, and Konstantinos N. Plataniotis. CL-DPS: A contrastive learning approach to blind nonlinear inverse problem solving via diffusion posterior sampling. In *The Fourteenth International Conference on Learning Representations*, 2026.

- Martin Zach, Youssef Haouchat, and Michael Unser. A statistical benchmark for diffusion-posterior-sampling algorithms. In *The Fourteenth International Conference on Learning Representations*, 2026.
- Kai Zhang, Yawei Li, Wangmeng Zuo, Lei Zhang, Luc Van Gool, and Radu Timofte. Plug-and-play image restoration with deep denoiser prior. *IEEE Trans. Pattern Anal. Mach. Intell.*, 44(10): 6360–6376, 2022.
- Richard Zhang, Phillip Isola, Alexei A Efros, Eli Shechtman, and Oliver Wang. The unreasonable effectiveness of deep features as a perceptual metric. In *Proceedings of the IEEE Conference on Computer Vision and Pattern Recognition*, pages 586–595, 2018.
- Hongkai Zheng, Wenda Chu, Bingliang Zhang, Zihui Wu, Austin Wang, Berthy Feng, Caifeng Zou, Yu Sun, Nikola Borislavov Kovachki, Zachary E Ross, Katherine Bouman, and Yisong Yue. Inversebench: Benchmarking plug-and-play diffusion priors for inverse problems in physical sciences. In *The 13th International Conference on Learning Representations*, 2025.
- Yuanzhi Zhu, Kai Zhang, Jingyun Liang, Jiezhong Cao, Bihan Wen, Radu Timofte, and Luc Van Gool. Denoising diffusion models for plug-and-play image restoration. In *Proceedings of the IEEE/CVF Conference on Computer Vision and Pattern Recognition*, pages 1219–1229, 2023.
- Zihao Zou, Jiaming Liu, Brendt Wohlberg, and Ulugbek S Kamilov. Deep equilibrium learning of explicit regularization functionals for imaging inverse problems. *IEEE Open J. Signal Process.*, 4: 390–398, 2023.

A Results on Natural Images

For natural images, the tasks include deblurring (Type I), random inpainting and $2\times$ super-resolution (Type II), and $4\times$ super-resolution (Type III). As training and in-distribution dataset, we consider CelebA-HQ [Karras et al., 2018]. For the evaluation, we further consider FFHQ [Karras et al., 2019] and AFHQ [Choi et al., 2020] as mild and completely out of distribution datasets, respectively. In contrast to the CT experiment from Section 4, we vary the evaluation data instead of the training data. Thus, we can execute all diffusion-based approaches with a model trained by Ho et al. [2020]². Quantitative results for both in-distribution and OOD settings are given in Table 2. Here, we also compare against the Reconstruct-Anything-Model (RAM) [Terris et al., 2026], a recently proposed foundation model for image reconstruction, in both a zero-shot approach and with their proposed finetuning routine using the validation data.

Table 2: Quantitative comparison across image restoration tasks for noise level $\sigma_n = 0.05$. The best value of each column is in bold and the second best is underlined. The hyperparameters of each method are chosen to maximize the PSNR on a validation set.

Method	CelebA-HQ (in-distribution)															
	Deblurring				Random Inpainting (60%)				$2\times$ Super-Resolution				$4\times$ Super-Resolution			
	PSNR \uparrow	SSIM \uparrow	LPIPS \downarrow	DC	PSNR \uparrow	SSIM \uparrow	LPIPS \downarrow	DC	PSNR \uparrow	SSIM \uparrow	LPIPS \downarrow	DC	PSNR \uparrow	SSIM \uparrow	LPIPS \downarrow	DC
RAM (zero-shot)	31.22	<u>0.873</u>	0.146	0.989	32.28	0.893	0.151	1.053	28.98	0.843	0.247	1.068	19.36	0.678	0.483	4.067
RAM (self-superv.)	31.17	0.864	0.193	0.996	34.01	<u>0.923</u>	0.089	0.979	<u>30.20</u>	<u>0.846</u>	0.236	0.978	25.38	0.725	0.393	1.012
PnP-LSR	<u>31.43</u>	0.869	0.188	0.981	34.23	0.924	0.059	0.905	29.92	0.838	0.267	0.969	25.99	0.732	0.407	0.939
WCRR	30.60	0.844	0.166	0.959	33.33	0.911	0.092	0.949	29.45	0.821	0.303	0.924	25.29	0.704	0.486	0.952
LSR	31.20	0.855	0.150	0.925	33.86	0.914	0.067	0.889	29.96	0.836	0.261	0.937	25.73	0.719	0.420	0.909
DiffPIR	30.57	0.841	<u>0.059</u>	0.982	31.78	0.885	<u>0.051</u>	1.005	29.75	0.833	<u>0.075</u>	0.980	<u>26.86</u>	<u>0.763</u>	<u>0.106</u>	0.951
DMPPlug	28.19	0.786	0.194	1.108	30.22	0.840	0.169	1.154	28.48	0.766	0.193	1.103	26.14	0.658	0.262	1.047
DPS	30.28	0.839	0.056	0.987	32.86	0.901	0.038	0.950	28.72	0.797	0.070	0.943	25.84	0.717	0.097	0.924
RED-diff	30.58	0.837	0.103	0.955	32.35	0.852	0.079	0.737	<u>30.20</u>	0.843	0.190	0.942	26.69	0.746	0.290	0.874
PnP-Flow	32.00	0.877	0.104	0.971	<u>34.15</u>	0.920	0.052	0.890	30.59	0.852	0.194	0.944	27.01	0.764	0.295	0.940
Method	CelebA-HQ \rightarrow FFHQ (medium out-of-distribution)															
	Deblurring				Random Inpainting (60%)				$2\times$ Super-Resolution				$4\times$ Super-Resolution			
	PSNR \uparrow	SSIM \uparrow	LPIPS \downarrow	DC	PSNR \uparrow	SSIM \uparrow	LPIPS \downarrow	DC	PSNR \uparrow	SSIM \uparrow	LPIPS \downarrow	DC	PSNR \uparrow	SSIM \uparrow	LPIPS \downarrow	DC
RAM (zero-shot)	29.92	0.855	0.154	0.987	30.90	0.876	0.157	1.070	27.61	<u>0.818</u>	0.280	1.061	19.04	0.641	0.528	4.009
RAM (self-superv.)	29.62	0.841	0.210	0.999	32.50	0.910	0.089	0.980	28.52	0.822	0.258	0.977	23.94	0.686	0.456	1.065
PnP-LSR	<u>29.88</u>	<u>0.847</u>	0.201	0.981	<u>32.44</u>	<u>0.908</u>	0.059	0.902	28.21	0.812	0.299	0.966	<u>24.63</u>	<u>0.694</u>	0.456	0.934
WCRR	28.89	0.815	0.193	0.961	31.08	0.881	0.081	0.910	27.69	0.790	0.348	0.927	24.08	0.666	0.540	0.959
LSR	29.44	0.827	0.181	0.960	31.68	0.889	0.082	0.896	28.05	0.796	0.305	0.912	24.46	0.684	0.474	0.908
DiffPIR	28.18	0.785	<u>0.119</u>	0.989	29.14	0.832	0.088	0.957	27.28	0.761	<u>0.163</u>	0.939	24.21	0.670	<u>0.225</u>	0.964
DMPPlug	24.53	0.685	0.297	1.290	26.04	0.739	0.266	1.419	25.10	0.694	0.283	1.321	23.31	0.596	0.321	1.159
DPS	27.94	0.778	0.118	0.980	29.91	0.847	<u>0.071</u>	0.949	26.67	0.740	0.147	0.932	23.49	0.621	0.208	0.913
RED-diff	28.02	0.731	0.190	0.906	29.35	0.760	0.115	0.647	27.31	0.786	0.269	0.960	24.28	0.668	0.378	0.883
PnP-Flow	29.70	0.837	0.142	0.974	31.37	0.883	<u>0.071</u>	0.904	<u>28.36</u>	0.811	0.245	0.942	25.28	0.717	0.350	0.940
Method	CelebA-HQ \rightarrow AFHQ (severely out-of-distribution)															
	Deblurring				Random Inpainting (60%)				$2\times$ Super-Resolution				$4\times$ Super-Resolution			
	PSNR \uparrow	SSIM \uparrow	LPIPS \downarrow	DC	PSNR \uparrow	SSIM \uparrow	LPIPS \downarrow	DC	PSNR \uparrow	SSIM \uparrow	LPIPS \downarrow	DC	PSNR \uparrow	SSIM \uparrow	LPIPS \downarrow	DC
RAM (zero-shot)	28.04	0.794	0.255	0.982	29.14	0.825	0.268	1.103	26.29	<u>0.737</u>	0.429	1.053	18.91	0.544	0.676	3.892
RAM (self-superv.)	27.64	0.766	0.345	1.001	<u>30.62</u>	<u>0.881</u>	<u>0.116</u>	0.963	26.90	0.742	0.421	0.972	<u>23.22</u>	<u>0.591</u>	0.608	1.055
PnP-LSR	<u>27.80</u>	<u>0.775</u>	0.358	0.986	30.67	0.884	0.087	0.890	26.66	0.728	0.472	0.967	23.92	0.603	0.614	0.933
WCRR	27.46	0.765	0.303	0.961	29.50	0.856	0.158	0.960	26.50	0.720	0.492	0.927	23.48	0.577	0.674	0.961
LSR	27.74	0.771	0.302	0.964	29.94	0.864	0.125	0.894	26.70	0.731	<u>0.463</u>	0.941	<u>23.80</u>	<u>0.599</u>	0.630	0.915
DiffPIR	26.04	0.689	<u>0.266</u>	0.987	27.09	0.769	0.206	0.967	25.72	0.683	0.324	0.993	22.86	0.545	<u>0.460</u>	1.042
DMPPlug	22.98	0.546	0.532	1.411	23.66	0.583	0.528	1.781	23.27	0.539	0.525	1.509	22.07	0.465	0.564	1.208
DPS	25.74	0.681	0.275	0.990	27.81	0.803	0.148	0.955	24.81	0.632	<u>0.329</u>	0.929	21.97	0.481	0.438	1.011
RED-diff	26.54	0.691	0.315	0.912	28.54	0.780	0.152	0.757	26.07	0.704	0.484	0.969	23.46	0.575	0.649	0.887
PnP-Flow	27.72	0.771	0.285	0.978	29.71	0.855	0.122	0.906	<u>26.71</u>	0.731	0.435	0.941	23.92	0.598	0.605	0.945

A.1 In-Distribution Performance (CelebA-HQ)

The in-distribution performance is given in the first part of Table 2. For the Type I & II problems, the forward operator \mathbf{A} is identifiable. Here, diffusion-based methods consistently achieve superior perceptual quality, as reflected by significantly lower LPIPS scores across all tasks. In particular, DPS achieves the best LPIPS in most identifiable settings, indicating a high perceptual quality. However, this comes at the cost of a worse PSNR and SSIM. The learned regularizers WCRR and LSR remain highly competitive, and are often superior in terms of PSNR and SSIM. Notably, LSR achieves the best PSNR and SSIM for random inpainting. Further, the fine-tuned RAM model also obtains a

²<https://huggingface.co/google/ddpm-ema-celebahq-256>

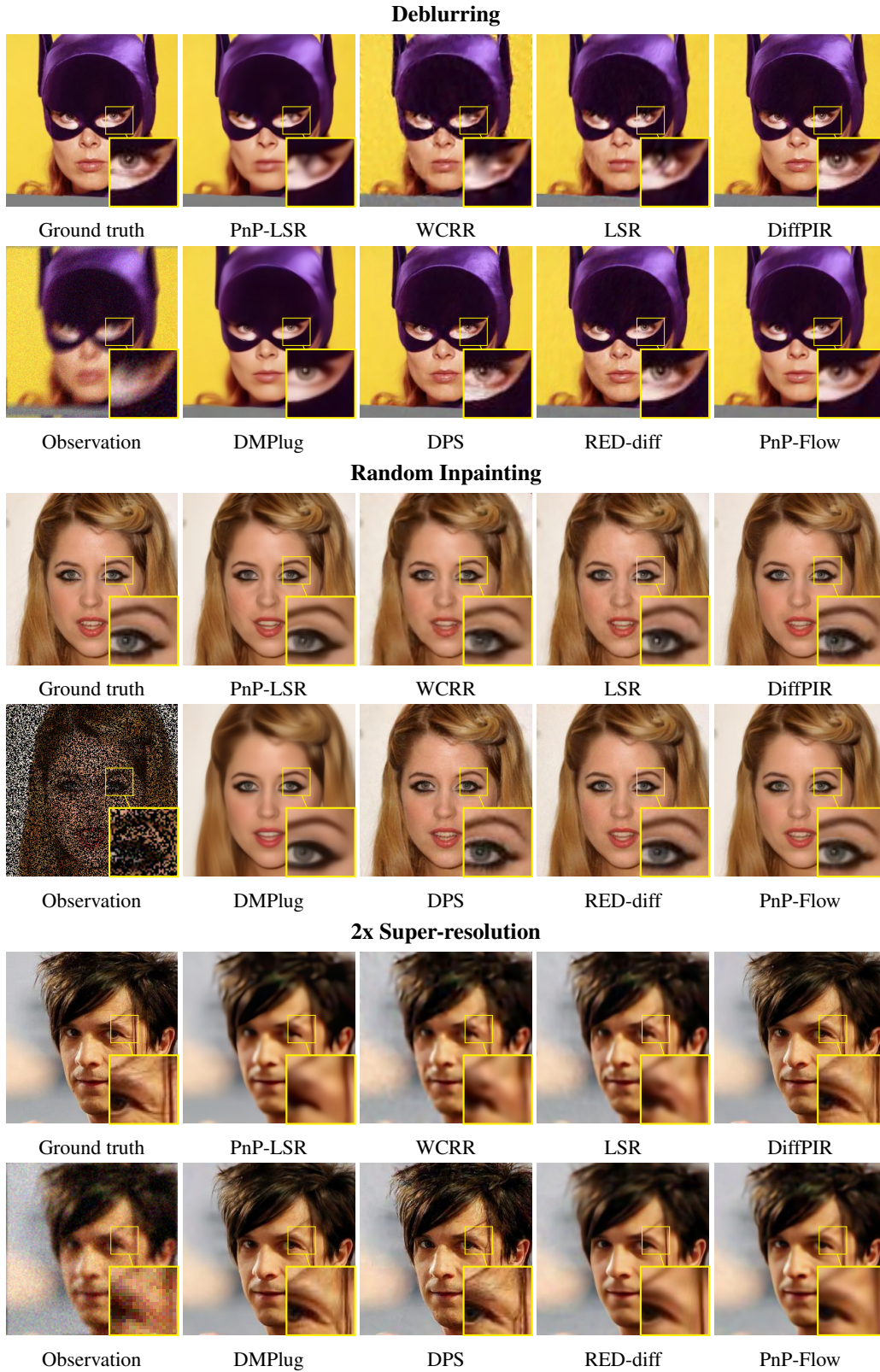


Figure 7: Quantitative reconstruction examples for Type I and II problems. The diffusion models lead to the most realistic looking results as also reflected by the high perceptual metrics in Table 2.

4x Super-resolution

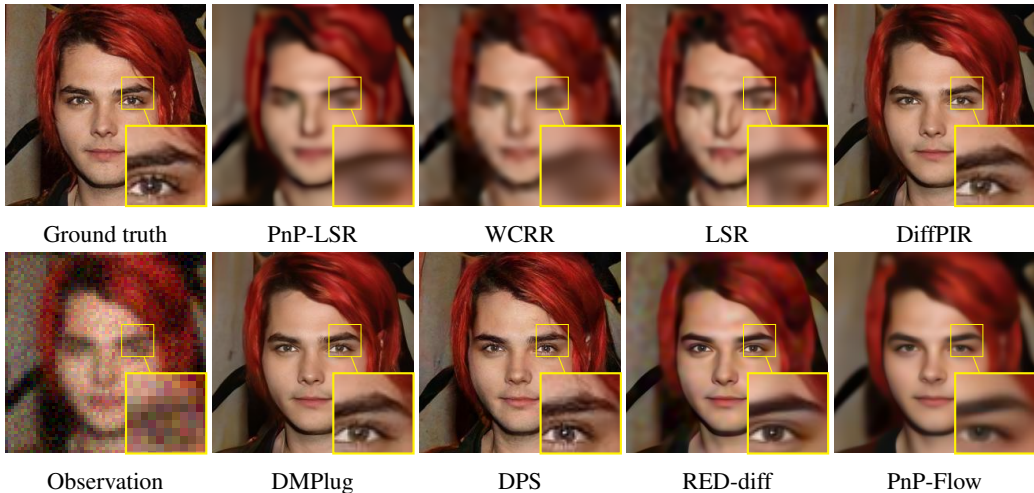


Figure 8: Quantitative reconstruction examples for a Type III problem. Large differences are for example visible in the background, around the eyes (magnified part), or in the hair.

comparable PSNR and SSIM to the LSR, albeit with a worse perceptual quality (as measured by the LPIPS) than the diffusion-based methods. Qualitative examples are provided in Figure 7. The visual differences are rather subtle and the reconstruction quality of all methods is generally high.

At $4\times$ super-resolution, the problem becomes non-identifiable due to a large nullspace $N(\mathbf{A})$ containing high-frequency components. Here, diffusion models clearly dominate, both in terms of quantitative metrics and the qualitative examples given in Figure 8. Methods such as DiffPIR and DPS achieve substantially lower LPIPS scores, indicating more realistic textures and structures. For example, DiffPIR achieves an LPIPS of 0.106, compared to 0.486 for WCRR. The larger differences in the metrics are also reflected by larger visual differences in the qualitative results. For this particular example, RED-diff cannot hold up with the other diffusion-based approaches.

A.2 Out-of-Distribution Generalization

To evaluate the robustness quantitatively, we applied the models trained on CelebA-HQ to images from FFHQ (medium OOD) and AFHQ (severely OOD), see the second and third part of Table 2. Across all methods and tasks, the performance degrades under the distribution shift. All diffusion models exhibit a high drop in performance, particularly in perceptual quality. While they remain competitive in LPIPS, the gap to the learned regularizers WCRR and LSR narrows significantly. This suggests that simpler priors with fewer parameters are less sensitive to distribution mismatch.

Figure 9 illustrates a key advantage of generative priors for Type III problems such as (large) box inpainting. In the chosen setting, the task is to fill in a large region of the face. Here, the diffusion-based methods DPS and DiffPIR produce visually coherent and semantically meaningful completions. In contrast, WCRR and LSR produces only smooth but unrealistic fillings, lacking semantic structure.

On the other hand, the generative strength of diffusion-based methods becomes a liability under distribution shift. When applied to OOD data from the AFHQ, diffusion-based approaches frequently generate (incorrect) structure aligned with their training distribution. As shown in Figure 9, DiffPIR might reconstruct a human face in place of a missing region in a cat image. For the learned regularizers WCRR and LSR, the outputs remain consistent with the observed data, albeit overly smooth and unrealistic. This makes it easy to identify these cases as failures.

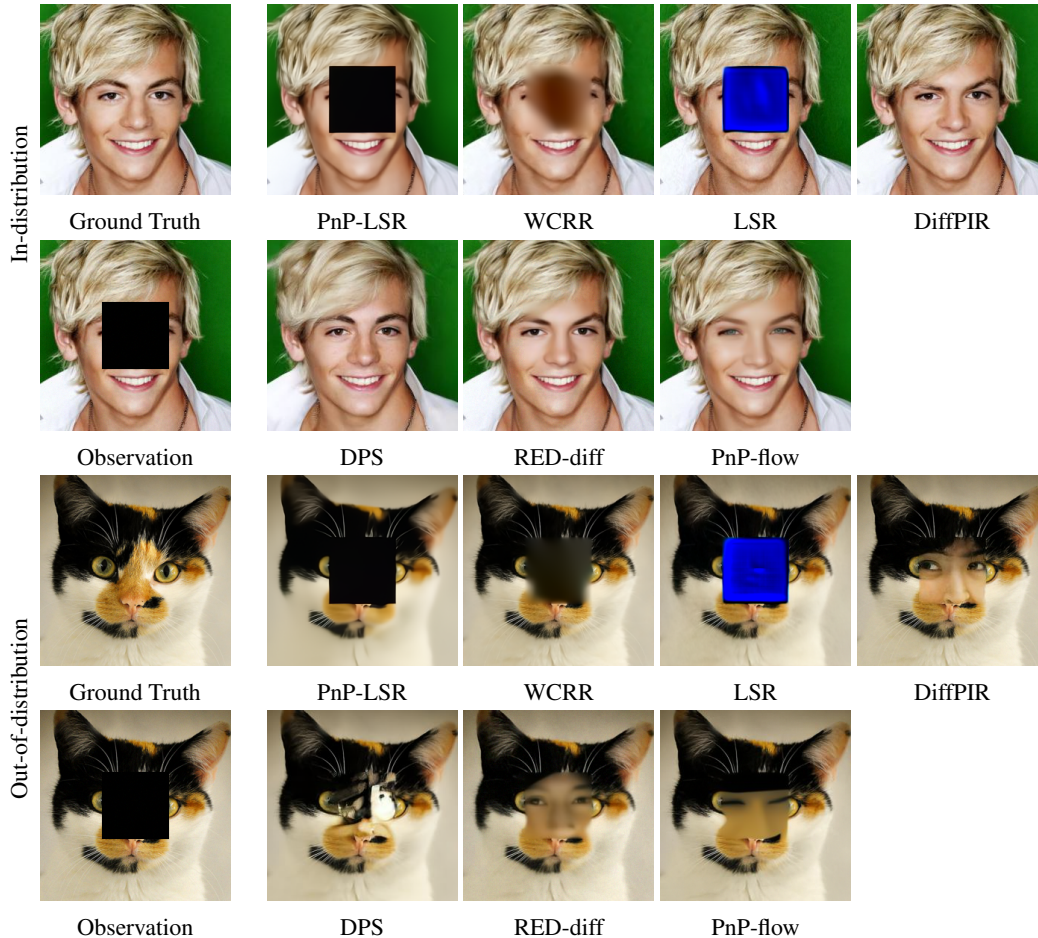


Figure 9: Box inpainting on in-distribution data (CelebA-HQ) and OOD data (AFHQ). For in-distribution data, the generative priors generate realistic looking images, while they fail for OOD data. For example, DiffPIR creates a human face for the cat. All learned regularizers simply fill in the missing region smoothly.

B Additional Results on CT

Here, we provide additional evidence and material for the CT experiment in Section 4.

B.1 Expanded Tables and Figures from the Main Body

In Table 3, we provide the metrics for the experiment visualized in Figure 3. Aside from the visualized PSNR, we also provide all SSIM, LPIPS and the data consistency (DC). The latter is strongly correlated with PSNR and should remain bounded if the reconstruction method is convergent. This is not the case for DPS and to some extent for RED-diff.

The extension of Figure 2 in the main body is provided in Figure 11. The visual differences are significant for 8 and 16 angles, namely the Type III setting. All (learned) regularizers tend to smooth out the reconstruction, whereas the generative models produce sharp results. However, the generated structure does not have anything in common with the actual ground truth.

In Table 4, we provide the metrics for the OOD experiment, which are visualized as a bar chart in Figure 5. The overall picture remains the same, namely that the (simple) learned regularizers degrade less under distribution shifts.

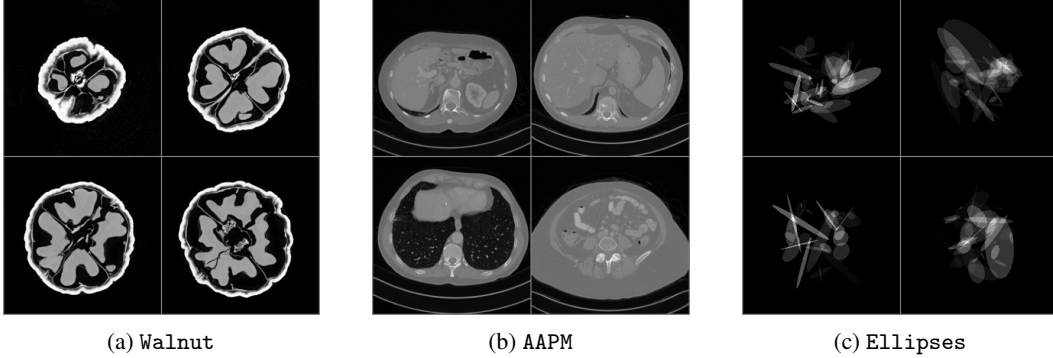


Figure 10: Example images from the Walnut, AAPM and Ellipses dataset.

Table 3: Vanishing noise level for parallel-beam CT with 128 angles. The best value of each column is in bold and the second best is underlined. The hyperparameters of each method are chosen to maximize the PSNR on a validation set. Raw data for Figure 3.

Method	$\sigma_n = 0.005$				Walnut \rightarrow Walnut (in-distribution)				$\sigma_n = 0.001$				$\sigma_n = 0$			
	PSNR \uparrow	SSIM \uparrow	LPIPS \downarrow	DC	PSNR \uparrow	SSIM \uparrow	LPIPS \downarrow	DC	PSNR \uparrow	SSIM \uparrow	LPIPS \downarrow	DC	PSNR \uparrow	SSIM \uparrow	LPIPS \downarrow	DC
FBP	25.00	0.463	0.475	0.541	29.21	0.671	0.280	1.016	30.37	0.745	0.231	2.709	30.85	0.776	0.214	-
TV	31.29	0.939	0.044	0.850	35.27	0.967	0.013	0.738	38.28	<u>0.980</u>	<u>0.006</u>	0.680	42.61	0.992	0.004	-
PnP-LSR	34.39	0.934	0.028	0.829	38.29	0.967	0.018	0.769	40.77	0.974	0.011	0.571	44.57	0.989	<u>0.005</u>	-
WCRR	33.80	0.930	0.032	0.819	37.93	<u>0.970</u>	0.020	0.775	40.58	0.978	0.010	0.589	<u>45.54</u>	0.992	0.004	-
LSR	<u>36.02</u>	0.932	0.025	0.943	<u>39.64</u>	0.967	0.016	0.815	<u>41.87</u>	0.978	0.011	0.704	45.76	<u>0.991</u>	0.004	-
DiffPIR	34.09	<u>0.955</u>	0.011	0.996	38.06	0.968	0.005	0.837	39.88	0.974	0.005	0.714	41.13	0.986	0.004	-
DPS	27.21	0.761	0.086	5.576	27.27	0.740	0.087	33.68	27.26	0.742	0.086	130.7	27.10	0.742	0.088	-
RED-diff	34.16	0.911	0.024	0.890	37.27	0.961	0.009	1.404	37.88	0.969	0.011	4.322	38.12	0.973	0.012	-
PnP-Flow	36.22	0.967	<u>0.014</u>	0.919	39.94	0.978	<u>0.007</u>	0.829	42.33	0.985	0.005	0.743	45.37	0.992	<u>0.005</u>	-

Lastly, the extension of Figure 6 in the main paper is given in Figure 12. For less informative measurements, the generative priors (and to some extent also the learned regularizers) show a strong bias towards their training distribution. This is particularly pronounced for the Ellipses data set.

B.2 Stability Regarding Different Noise Realizations

To evaluate the robustness of the reconstruction methods against (small) perturbations of the measurements, we perform a stability analysis across different noise realizations. For this, we consider the sparse-view CT setting with 16 projection angles and a noise level of $\sigma_n = 0.01$. The evaluation is conducted on 10 in-distribution images (indices 0,10,...,90), where for each one, we compute reconstructions for 40 independent noise realizations. We report the average and maximal standard deviations for PSNR, SSIM, LPIPS, and Data Consistency (DC) in Table 5. Unsurprisingly, the sampling based approach DPS shows the highest variance, whereas the simple regularizers TV and WCRR are both very robust for the distortion metrics PSNR and SSIM.

B.3 Regularization Strength Dynamics

The regularization strength λ (or data consistency parameter γ) controls the trust that we put in our data. Figure 13 illustrates how reconstruction quality varies if we change these parameters. We emphasize that we vary only the regularization strength, leaving all other hyperparameters fixed; in particular, the primal-dual solver for TV was not retuned. In principle, the behavior is intuitive: large regularization strength pushes the solution toward the prior (i.e., the Ellipses dataset), while weak regularization approaches a least-squares solution for methods with an explicit data consistency term. Indeed, all generative methods produce ellipse-like images for sufficiently large regularization strength—with DiffPIR being the only exception that retains some structural fidelity to the walnut. Interestingly, in the low-regularization regime, DPS eventually degenerates to noise.

Table 4: Quantitative comparison for CT reconstruction tasks with additive Gaussian noise ($\sigma_n = 0.01$). The best value of each column is in bold and the second best is underlined. Hyperparameters are chosen to maximize PSNR on a validation set. Raw data for Figure 5.

Method	AAPM \rightarrow Walnut (out-of-distribution)								Ellipses \rightarrow Walnut (out-of-distribution)							
	Sparse View (32 angles)				Sparse View (128 angles)				Sparse View (32 angles)				Sparse View (128 angles)			
	PSNR \uparrow	SSIM \uparrow	LPIPS \downarrow	DC	PSNR \uparrow	SSIM \uparrow	LPIPS \downarrow	DC	PSNR \uparrow	SSIM \uparrow	LPIPS \downarrow	DC	PSNR \uparrow	SSIM \uparrow	LPIPS \downarrow	DC
WCRR	28.27	0.874	0.091	0.689	29.66	0.912	<u>0.093</u>	0.944	27.44	0.896	0.066	0.648	29.04	0.926	0.055	0.947
LSR	<u>26.61</u>	<u>0.840</u>	<u>0.141</u>	0.787	<u>29.48</u>	<u>0.899</u>	0.062	0.936	<u>25.17</u>	<u>0.871</u>	<u>0.101</u>	0.743	<u>26.53</u>	<u>0.889</u>	<u>0.082</u>	0.902
DiffPIR	21.44	0.345	0.537	0.353	24.85	0.521	0.429	0.889	24.70	0.704	0.228	0.405	<u>27.11</u>	0.838	0.129	0.867
DPS	19.38	0.281	0.615	20.872	21.63	0.398	0.553	4.914	23.86	0.825	0.163	1.223	25.50	0.823	0.129	1.268
RED-diff	21.61	0.356	0.516	0.396	25.08	0.523	0.423	0.802	24.01	0.578	0.298	0.349	26.07	0.633	0.253	0.770
PnP-Flow	22.38	0.447	0.437	0.649	25.51	0.611	0.358	0.933	24.08	0.763	0.198	0.636	26.33	0.848	0.138	0.890

Method	CelebA-HQ \rightarrow Walnut (out-of-distribution)							
	Sparse View (32 angles)				Sparse View (128 angles)			
	PSNR \uparrow	SSIM \uparrow	LPIPS \downarrow	DC	PSNR \uparrow	SSIM \uparrow	LPIPS \downarrow	DC
WCRR	26.47	0.848	0.141	0.809	29.01	0.858	0.109	0.915
LSR	29.37	<u>0.873</u>	<u>0.070</u>	0.614	30.16	0.915	<u>0.077</u>	0.949
DiffPIR	<u>27.57</u>	0.876	0.067	0.866	<u>29.20</u>	<u>0.901</u>	0.047	0.966
DPS	24.01	0.719	0.225	0.943	24.58	0.753	0.206	1.326
RED-diff	25.83	0.646	0.242	0.422	27.93	0.729	0.181	0.861
PnP-Flow	24.09	0.597	0.394	0.643	26.65	0.635	0.311	0.803

Table 5: Stability analysis across 40 independent noise realizations for sparse-view CT (16 angles, noise level $\sigma_n = 0.01$). We report the average and maximal standard deviation for each metric. The best value of each column is in bold and the second best is underlined (except for DC).

Method	Average Standard Deviation				Maximal Standard Deviation			
	PSNR	SSIM	LPIPS	DC	PSNR	SSIM	LPIPS	DC
TV	0.0544	<u>0.0027</u>	0.0039	0.0126	0.0725	0.0032	0.0051	0.0147
PnP-LSR	0.3061	0.0291	0.0204	0.0962	0.4264	0.0411	0.0272	0.1146
WCRR	<u>0.1482</u>	<u>0.0028</u>	<u>0.0028</u>	0.0158	0.2255	<u>0.0037</u>	0.0038	0.0176
LSR	0.3095	0.0032	0.0028	0.0117	0.4691	<u>0.0055</u>	0.0055	0.0127
DiffPIR	0.2763	0.0034	0.0031	0.0126	0.4326	0.0042	0.0100	0.0168
DPS	0.5049	0.0158	0.0351	1.1050	1.0421	0.0416	0.0552	5.2854
RED-diff	0.1624	0.0053	<u>0.0022</u>	0.0686	<u>0.1998</u>	0.0059	<u>0.0030</u>	0.1127
PnP-Flow	0.2030	0.0023	0.0015	0.0134	0.7517	0.0069	0.0022	0.0166

B.4 Latent Diffusion Models for Inverse Problems

Large-scale text-to-image diffusion and flow models are increasingly adopted for solving inverse problems [Kim et al., 2025, Erbach et al., 2026, Webber et al., 2026]. These approaches build on powerful pretrained generative backbones such as Stable Diffusion 3.0 (SD 3.0) [Esser et al., 2024] or FLUX.2 [Labs, 2025]. Most existing evaluations focus on natural image restoration, closely aligned with the benchmarks discussed in Appendix A. Here, we study the behavior in sparse-view CT.

For this, a major challenge is that SD 3.0 and FLUX.2 operate in latent space. This distinction from classical pixel-space diffusion has important consequences for enforcing data consistency. More precisely, the data-consistency term appearing in many reconstruction algorithms now takes the form $\|\mathbf{A}D(\mathbf{z}_t) - \mathbf{y}\|^2$, where D denotes the decoder that maps latent variables \mathbf{z}_t to image space. As a result, the corresponding data-consistency updates become non-convex optimization problems, which are considerably harder to solve than the quadratic problems arising in pixel-space diffusion.

As representative method, we adapt Flow-DPS [Kim et al., 2025]. Originally, Flow-DPS was only evaluated for natural images, where the authors use 3 steps of gradient descent with a fixed step size (15.0) to minimize the data consistency step in each sampling iteration (see Appendix 8 in Kim et al. [2025]). While effective in their setting, we find it insufficient to enforce data consistency in CT. Thus, we use up to 50 data consistency steps with an early stopping rule based on the noise level $\|\mathbf{A}\mathbf{x} - \mathbf{y}\|^2 \leq \delta^2$. Moreover, we use 28 timesteps, classifier-free guidance scaling of 2.0, and the prompt ‘‘a computed tomography image of a walnut’’.

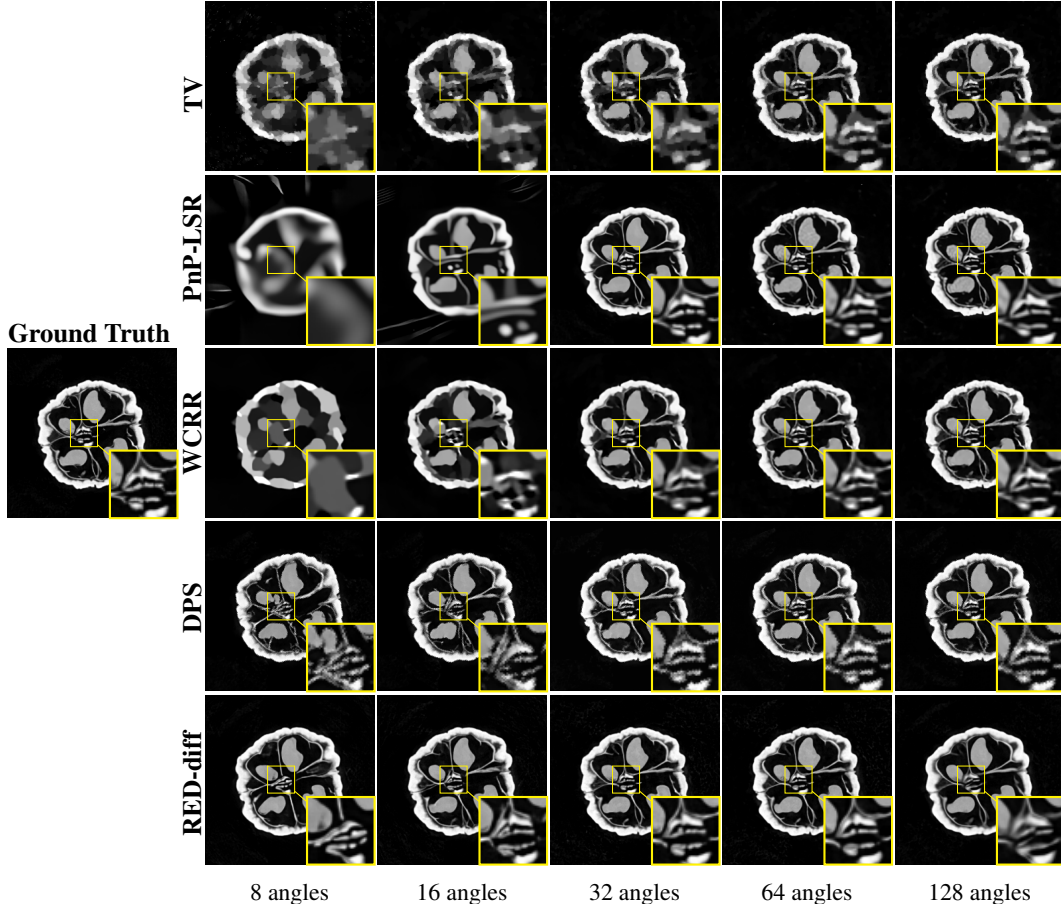


Figure 11: Reconstruction of a walnut slice for various number of angles. While being of Type I/II for 128 angles, the task is very hard (Type III) for only 8 angles. This is underlined by the hallucinations (artificial structures) that are visible in the magnified square. Extension of Figure 2 in the main paper.

Table 6 summarizes the quantitative results for sparse-view CT with 32 and 128 angles and additive Gaussian noise ($\sigma_n = 0.01$) as described in Section 4.1. We observe that despite the large model size, Flow-DPS performs worse than the in-distribution version DiffPIR (Walnut). Actually, it performs even worse than DiffPIR trained on CelebA-HQ. Figure 14 compares reconstructions for the different methods. Here, we observe that the Flow-DPS reconstruction is overly smooth compared to the in-distribution DiffPIR (Walnut) reconstruction.

B.5 Misspecified Forward Operator and Noise Model

In practice, the forward operator \mathbf{A} and the noise statistics are rarely known exactly. Thus, we introduce a controlled misspecification in both to evaluate robustness for the setting from Section 4.1.

1. **Forward operator mismatch:** Let \mathbf{A}_ϕ denote the forward operator parametrized by projection angles $\phi = [\phi_1, \dots, \phi_n]$. The measured data \mathbf{y} is generated using a perturbed set of angles $\psi = [\psi_1, \dots, \psi_n]$, where $\psi_i = \phi_i + \epsilon_i$ with $\epsilon_i \sim \mathcal{U}(-0.7^\circ, 0.7^\circ)$. For reconstruction, we make use of the operator \mathbf{A}_ϕ introducing a model mismatch.
2. **Noise model mismatch:** The reconstruction methods assume additive Gaussian noise of the form $y^\delta = y + \delta\eta$ with $\eta \sim \mathcal{N}(0, I)$, where $\delta > 0$ controls the noise level. Instead, we corrupt the actual measurements by signal-dependent noise

$$y^\delta = y + \delta\sqrt{|y|}\eta, \quad \eta \sim \mathcal{N}(0, I).$$

The parameter δ is chosen such that the overall noise variance is comparable to the additive Gaussian case, ensuring a fair comparison while still inducing a noise mismatch.

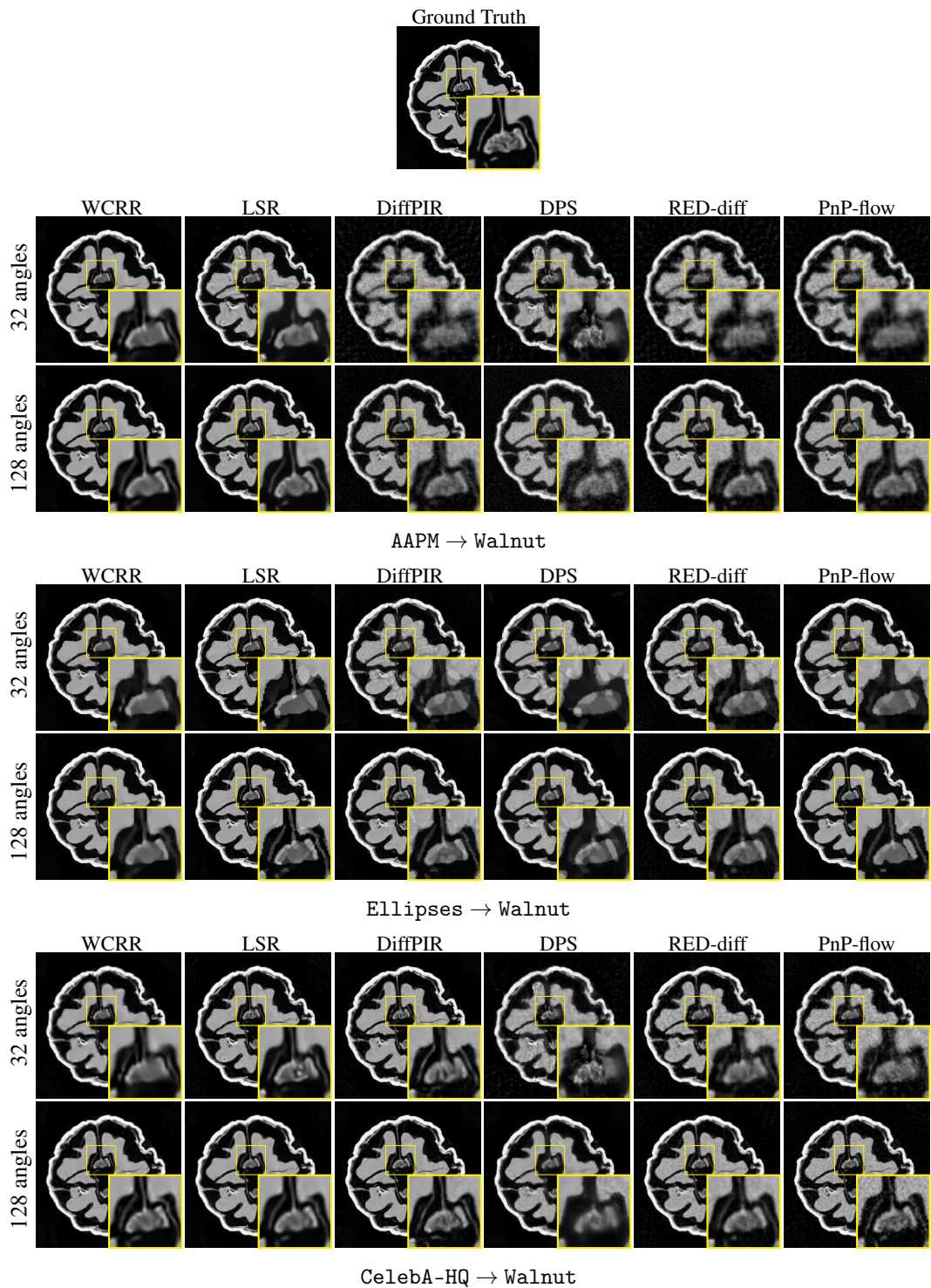


Figure 12: Reconstruction of a walnut slice for the OOD settings considered in Table 4 with 128 angles. Extension to Figure 6 in the main paper.

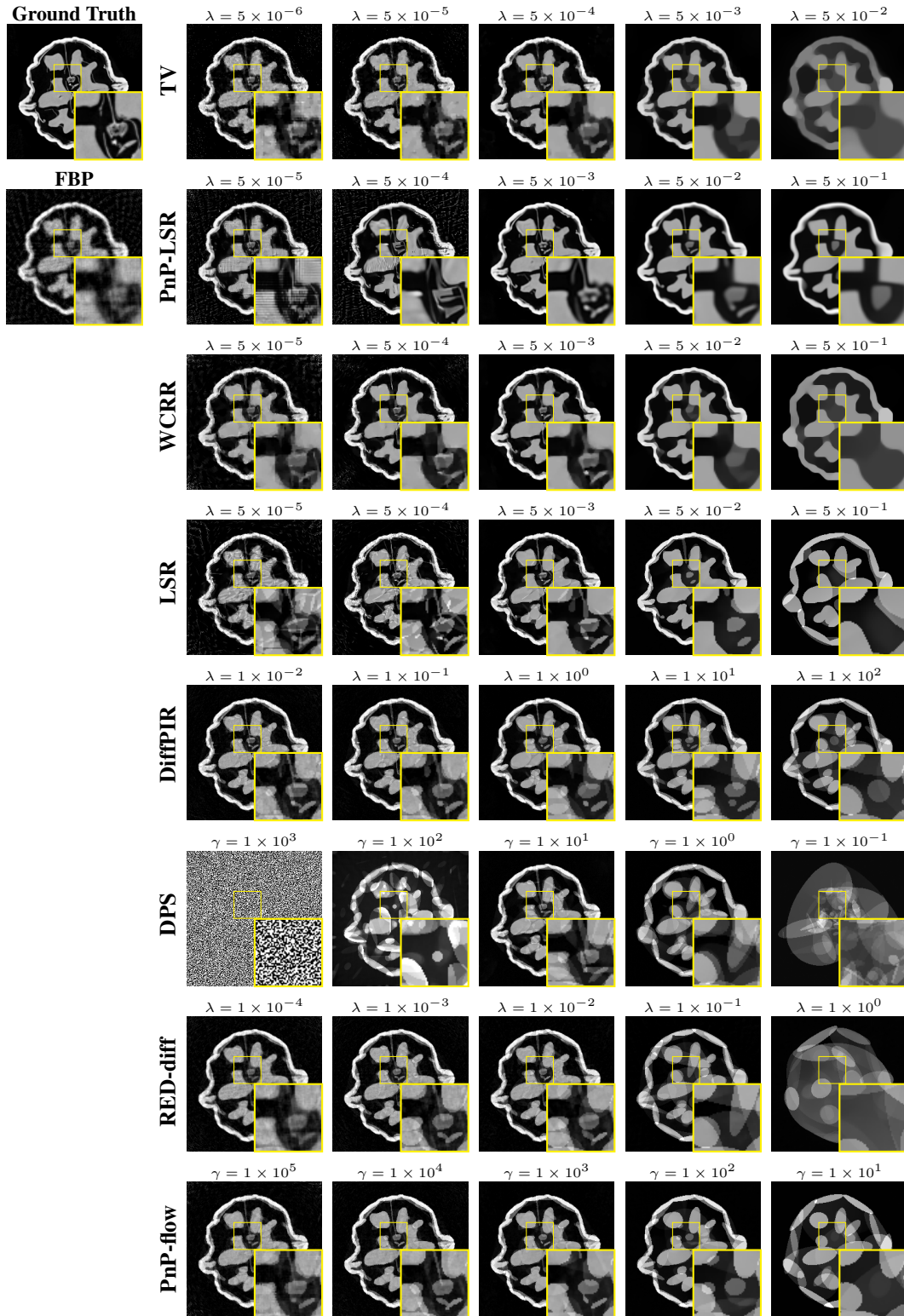


Figure 13: Reconstruction for the 32 angle CT setting with various choices of the regularization or data consistency parameter, respectively. All data-based methods are trained on the Ellipses dataset. The prior becomes clearly visible for large regularization strength.

Table 6: Quantitative comparison for CT reconstruction tasks with additive Gaussian noise ($\sigma_n = 0.01$) for text-to-image latent flow models compared to the pixel space diffusion models. The best value of each column is in bold and the second best is underlined (except for DC).

Method	Sparse View (32 angles)				Sparse View (128 angles)			
	PSNR \uparrow	SSIM \uparrow	LPIPS \downarrow	DC	PSNR \uparrow	SSIM \uparrow	LPIPS \downarrow	DC
Flow-DPS (SD 3.0)	26.78	0.871	0.098	1.752	27.78	0.885	0.086	1.181
DiffPIR (Walnut)	30.90	0.929	0.020	0.795	31.85	0.939	0.015	0.957
DiffPIR (AAPM)	21.44	0.345	0.537	0.353	24.85	0.521	0.429	0.889
DiffPIR (Ellipses)	24.70	0.704	0.228	0.405	27.11	0.838	0.129	0.867
DiffPIR (CelebA-HQ)	<u>27.57</u>	<u>0.876</u>	<u>0.067</u>	0.866	<u>29.20</u>	<u>0.901</u>	<u>0.047</u>	0.966

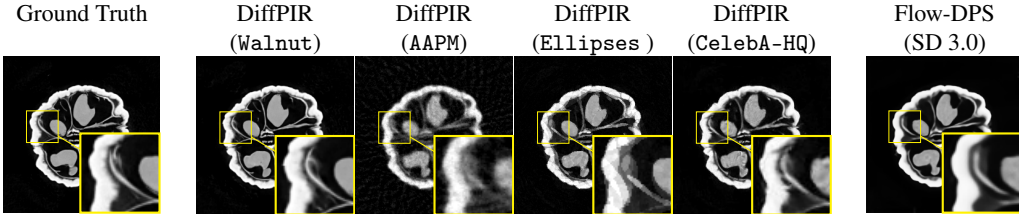


Figure 14: Reconstructions for Flow-DPS (SD 3.0) and DiffPIR in the 32-angle setting.

Table 7: Misaligned evaluation settings. Hyperparameters are the same as in Table 1 (no additional search). The best value of each column is in bold and the second best is underlined.

Method	Misaligned Angles						Misaligned Noise Model					
	Sparse View (32 angles)			Sparse View (128 angles)			Sparse View (32 angles)			Sparse View (128 angles)		
	PSNR \uparrow	SSIM \uparrow	LPIPS \downarrow	PSNR \uparrow	SSIM \uparrow	LPIPS \downarrow	PSNR \uparrow	SSIM \uparrow	LPIPS \downarrow	PSNR \uparrow	SSIM \uparrow	LPIPS \downarrow
FBP	15.32	0.230	0.591	19.69	0.311	0.667	14.21	0.204	0.658	19.88	0.320	0.625
TV	25.47	0.832	0.130	27.77	0.876	0.102	25.32	0.855	0.180	27.89	0.893	0.121
PnP-LSR	26.99	0.843	0.127	29.39	0.837	0.106	27.29	0.877	0.117	28.72	0.859	0.106
WCRR	26.99	0.813	0.086	29.33	0.833	0.073	26.13	0.870	0.098	29.50	0.886	0.062
LSR	<u>28.62</u>	0.853	0.060	<u>31.47</u>	0.878	0.043	28.81	0.853	0.058	<u>32.03</u>	0.879	0.038
DiffPIR	28.31	0.878	<u>0.034</u>	30.79	0.928	0.020	28.88	0.924	0.026	30.12	0.933	<u>0.022</u>
DPS	24.92	0.732	0.106	27.16	0.881	0.079	25.12	0.735	0.110	26.82	0.801	0.089
RED-diff	27.62	0.730	0.086	27.17	0.841	0.076	28.26	0.798	0.077	27.47	0.879	0.064
PnP-Flow	28.96	0.914	0.033	31.90	0.939	<u>0.021</u>	29.82	0.933	<u>0.029</u>	32.31	0.948	0.021

Table 7 summarizes the quantitative results. The performance of all methods is degraded significantly, for example by around 1-2 dB in PSNR. Moreover, DPS now performs consistently worse than TV. Among the remaining methods, the best results are achieved with PnP-Flow, DiffPIR, and LSR.

C Further Discussions and Limitations

While we included the most important discussions and limitations in Section 5, there are more interesting aspects. In particular, we discuss the additional results from the Appendices A and B.

Generation Capabilities for Type III Problems In Figure 9 (box inpainting), we see that learned regularizers are unable to generate plausible content in Type III problems, where substantial parts of information are missing. For our experiments on natural images in Appendix A (see also Figure 7 and 8), we make similar observations for Type II/III problems. Here, diffusion priors generate much better results, particularly when considering perceptual metrics like LPIPS or the visual impression.

Takeaway: If substantial information is missing and must be filled with realistic content, variational methods (TV, WCRR, LSR) are insufficient; a generative prior is required.

Stability under Modeling Errors We have seen in Appendix B.5 that the diffusion priors and PnP-flow exhibit a better stability with respect to modeling errors (forward operator and noise model) compared to the learned regularizers. A likely explanation is that generative priors encode detailed knowledge of the data distribution, whereas variational methods primarily enforce structural properties such as smoothness and edge sharpness. While this distinction supports better generalization for variational methods (cf. Section 5), it makes them more sensitive to modeling errors.

Takeaway: If the precise prior distribution is known but the forward operator \mathbf{A} and the noise model are uncertain, generative priors (DiffPIR, PnP-flow) are preferable over learned regularizers.

Natural vs Scientific Imaging Comparing the scientific imaging experiments (Section 4 and Appendix B) with the experiments on natural images (Appendix A), the overall conclusions differ: For natural images, all diffusion priors show a clear advantage in the Type III setting. For Type I/II problems, variational methods (WCRR, LSR, PnP-LSR) are competitive and sometimes even better in PSNR or SSIM. In contrast, for scientific imaging, most diffusion priors degrade, with only PnP-flow and DiffPIR remaining somehow competitive with variational methods. Although variational methods are more robust to OOD settings in both scenarios, this advantage is far more pronounced for scientific imaging. Overall, there appears to be a substantial performance gap for diffusion priors between natural and scientific imaging tasks.

Takeaway: The performance of reconstruction methods can heavily depend on the considered image domains. Thus, benchmarks should consider both natural and scientific imaging settings or clearly state their limited scope.

Computation Time Figure 4 shows that reconstructions with generative priors are significantly slower than with TV, WCRR, or LSR, which is expected given their much larger model sizes. We note that we did not try to find the minimal model size for competitive reconstruction performance. The differences between DiffPIR and RED-diff are relatively small, as both require the same number of model evaluations. DPS, which differentiates through the score network, incurs an additional cost of roughly a factor of 1.5–2, which remains manageable. In contrast, DMPlug differentiates through the entire sampling trajectory, leading to substantial computational and memory overhead. Further, DiffPIR and (implicit) PnP-flow both rely on the proximal mapping of the data term, which becomes a bottleneck for nonlinear or expensive to evaluate forward operators.

Perspective: Our experiments suggest that diffusion priors and PnP-flow are much more expensive to deploy than the learned regularizers. A detailed comparison is left for future work.

Non-Linear Operators and Arbitrary Noise Few generative methods transfer directly to these regimes. For example, implicit PnP-flow and DiffPIR require computing the proximal mapping of the data term, which only simplifies to a linear solve for linear forward operators and quadratic (Gaussian) data terms. In general, solving the non-convex optimization problem might be untractable. Also for DPS and RED-diff it has been observed in the literature that they do not work well with non-linear forward operators [Denker et al., 2024, Ye et al., 2026]. Variational methods are generally free from this restriction. Still, the energy landscape of the variational problem (2) may become more complex, compromising global convergence guarantees for gradient-based minimization.

Perspective: While the variational methods (WCRR, LSR) can directly be transferred to non-linear forward operators and other noise models, this seems to be more involved for diffusion priors and (implicit) PnP-flow. A detailed comparison is left for future work.

Further Limitations First, our experiments are not designed to draw a detailed run time comparison. Figure 4 only gives a rough impression and only considers the time of generating a single image. In particular, further code optimizations and potential parallelization abilities are not considered. Second, we did not consider nonlinear forward operators or noise models different than the Gaussian one. Even though different noise levels are particularly relevant to scientific or medical imaging, we feel that this would be beyond the scope of our study. Finally, we restricted our analysis to point

estimation methods and did not address posterior sampling techniques. Although we believe that a stability analysis would also be valuable in that setting, it lies outside the scope of the present work. For related work in this direction, we refer to Thong et al. [2024], Zach et al. [2026].

Potential Societal Impact We investigate applications of conditional generation using diffusion and flow-based models. A central objective of this work is to identify and mitigate failure modes in these approaches, thereby improving the stability and reliability of reconstructions. This, in turn, has the potential to enhance the robustness of imaging pipelines. At the same time, conditional generation carries risks of misuse, including the creation of deepfakes or disinformation, as well as the production of plausible yet incorrect reconstructions (“hallucinations”) in imaging contexts. Such outputs may mislead practitioners if not carefully validated. However, our work does not extend existing generative capabilities; instead, it focuses on evaluating established methods. Further, we put significant emphasis on identifiable problems, where the risk of misuse is less dominant.

D Diffusion Models for Inverse Problems

In the following, we provide more details on how diffusion models can be used for solving inverse problems. The hyperparameter selection process and the found choices are discussed in Section F.5. Our presentation assumes additive Gaussian noise $\boldsymbol{\eta} \sim \mathcal{N}(\mathbf{0}, \sigma_y^2 \mathbf{I})$ with standard deviation $\sigma_y > 0$. For other noise types, the approaches often need to be adapted, e.g., Singh et al. [2024] adapt several posterior sampling strategies to inverse problems under Poisson noise. Throughout, we write all algorithms in terms of the diffusion model ϵ_θ . Instead, one can equivalently use the score model $\nabla_{\mathbf{x}_t} \log p_t(\mathbf{x}_t) \approx s_\theta(\mathbf{x}_t, t) := -\epsilon_\theta(\mathbf{x}_t, t) / \sqrt{1 - \bar{\alpha}_t}$.

D.1 Diffusion Posterior Sampling

Guidance-based methods, see Daras et al. [2024] for an overview, replace the unconditional process (3) with a posterior process targeting $p(\mathbf{x}_t | \mathbf{y})$. By Bayes’ rule, the conditional score decomposes as

$$\nabla_{\mathbf{x}_t} \log p_t(\mathbf{x}_t | \mathbf{y}) = \nabla_{\mathbf{x}_t} \log p_t(\mathbf{x}_t) + \nabla_{\mathbf{x}_t} \log p_t(\mathbf{y} | \mathbf{x}_t), \quad (4)$$

where the first term is the unconditional score, given by the diffusion model $\epsilon_\theta(\mathbf{x}_t, t)$, and the second one is a likelihood gradient that enforces measurement consistency. Since the likelihood $p(\mathbf{y} | \mathbf{x}_t)$ is intractable in general, Chung et al. [2023] propose to approximate it via the posterior mean and Tweedie’s formula, leading to the tractable likelihood gradient

$$\nabla_{\mathbf{x}_t} \log p_t(\mathbf{y} | \mathbf{x}_t) \approx -\frac{1}{\sigma_y^2} \nabla_{\mathbf{x}_t} \|\mathbf{y} - \mathbf{A}\hat{\mathbf{x}}_t(\mathbf{x}_t)\|^2, \quad (5)$$

where the denoised image $\hat{\mathbf{x}}_t(\mathbf{x}_t)$ is given by Tweedie’s formula as

$$\hat{\mathbf{x}}_t(\mathbf{x}_t) = \frac{1}{\sqrt{\bar{\alpha}_t}} (\mathbf{x}_t - \sqrt{1 - \bar{\alpha}_t} \epsilon_\theta(\mathbf{x}_t, t)). \quad (6)$$

After inserting (4) and (5), the reverse step (3) becomes

$$\mathbf{x}_{t-1} = \frac{1}{\sqrt{\alpha_t}} \left(\mathbf{x}_t - \frac{\beta_t}{\sqrt{1 - \bar{\alpha}_t}} \epsilon_\theta(\mathbf{x}_t, t) \right) + \sqrt{\beta_t} \boldsymbol{\epsilon}_t - \gamma_t \nabla_{\mathbf{x}_t} \|\mathbf{y} - \mathbf{A}\hat{\mathbf{x}}_t(\mathbf{x}_t)\|^2,$$

where $\gamma_t = \gamma / \|\mathbf{y} - \mathbf{A}\hat{\mathbf{x}}_t(\mathbf{x}_t)\|$ controls the strength of the data-consistency correction. Since $\nabla_{\mathbf{x}_t} \|\mathbf{y} - \mathbf{A}\hat{\mathbf{x}}_t(\mathbf{x}_t)\|^2$ is computed via automatic differentiation through $\hat{\mathbf{x}}_0(\mathbf{x}_t)$, the DPS approach allows to sample reconstructions for any differentiable forward operator \mathbf{A} . However, this requires backpropagation through $\epsilon_\theta(\mathbf{x}_t, t)$, which is computationally expensive. There exist several related methods using the score decomposition (4) but different estimates of the likelihood gradient, see e.g., Kawar et al. [2022], Wang et al. [2023]. The full approach is given in Algorithm 3. We always run DPS for $T = 1000$ sampling steps and the only tunable hyperparameter is the guidance scale γ .

D.2 Plug-and-Play with Diffusion Models

As a representative PnP method that relies on diffusion priors, we discuss DiffPIR [Zhu et al., 2023]. This approach adapts the half-quadratic splitting (HQS) algorithm to the reverse diffusion process (3).

Algorithm 1 DPS

Input: Observation \mathbf{y} , pre-trained diffusion model $\{\epsilon_\theta, \beta_t, \bar{\alpha}_t\}$ **Hyperparameters:** taken time steps T , guidance scale γ

- 1: Initialize $\mathbf{x}_T \sim \mathcal{N}(\mathbf{0}, \mathbf{I})$
 - 2: **for** $t = T$ **to** 1 **do**
 - 3: $\hat{\mathbf{x}}_t(\mathbf{x}_t) = (\mathbf{x}_t - \sqrt{1 - \bar{\alpha}_t} \epsilon_\theta(\mathbf{x}_t, t)) / \sqrt{\bar{\alpha}_t}$ ▷ Predict $\hat{\mathbf{x}}_t$ with score model as denoiser
 - 4: $\mathbf{g}_t = -\nabla_{\mathbf{x}_t} \|\mathbf{y} - \mathbf{A} \hat{\mathbf{x}}_t(\mathbf{x}_t)\|^2$ ▷ Compute gradient estimation
 - 5: $\gamma_t = \gamma / \|\mathbf{y} - \mathbf{A} \hat{\mathbf{x}}_t(\mathbf{x}_t)\|$ ▷ Calculate step size
 - 6: $\boldsymbol{\epsilon}_t \sim \mathcal{N}(\mathbf{0}, \mathbf{I})$
 - 7: $\mathbf{x}_{t-1} = \frac{1}{\sqrt{\bar{\alpha}_t}} (\mathbf{x}_t - \frac{\beta_t}{\sqrt{1 - \bar{\alpha}_t}} \epsilon_\theta(\mathbf{x}_t, t)) + \sqrt{\beta_t} \boldsymbol{\epsilon}_t - \gamma_t \mathbf{g}_t$
 - 8: **end for**
 - 9: **return** \mathbf{x}_0
-

Given a noisy sample \mathbf{x}_t at timestep t , DiffPIR performs the three updates

$$\mathbf{p}_t = (\mathbf{x}_t - \sqrt{1 - \bar{\alpha}_t} \epsilon_\theta(\mathbf{x}_t, t)) / \sqrt{\bar{\alpha}_t}, \quad (7)$$

$$\hat{\mathbf{x}}_t = \underset{\mathbf{x}}{\operatorname{argmin}} \|\mathbf{A} \mathbf{x} - \mathbf{y}\|^2 + \frac{\lambda \sigma_y^2 \bar{\alpha}_t}{(1 - \bar{\alpha}_t)} \|\mathbf{x} - \mathbf{p}_t\|^2, \quad (8)$$

$$\mathbf{x}_{t-1} = \sqrt{\bar{\alpha}_{t-1}} \hat{\mathbf{x}}_t + \sqrt{1 - \bar{\alpha}_{t-1}} \left(\frac{\sqrt{1 - \zeta}}{\sqrt{1 - \bar{\alpha}_t}} (\mathbf{x}_t - \sqrt{\bar{\alpha}_t} \hat{\mathbf{x}}_t) + \sqrt{\zeta} \boldsymbol{\epsilon}_t \right), \quad \boldsymbol{\epsilon}_t \sim \mathcal{N}(\mathbf{0}, \mathbf{I}). \quad (9)$$

The update (7) denoises the current reconstruction \mathbf{x}_t based on the estimate $\bar{\sigma}_t = \sqrt{(1 - \bar{\alpha}_t) / \bar{\alpha}_t}$, which is tailored to the diffusion schedule and decreases as $t \rightarrow 0$. For linear inverse problems, the update (8) admits a closed-form solution (or can be computed using a few steps of conjugate gradient with initialization \mathbf{p}_t). Unlike the classical HQS-PnP approach [Hurault, 2023], we have the update (9) that re-injects noise to move $\hat{\mathbf{x}}_t$ back onto the diffusion manifold at level $t - 1$ based on the effective noise residual implied by the data-consistent estimate $\hat{\mathbf{x}}_t$. This scheduling ensures that the noise level $\bar{\sigma}_t$ passed to the denoiser is always consistent with the current diffusion timestep. The authors suggest $T = 100$ steps for natural imaging. For CT, we found that $T = 1000$ increases the performance. In summary, DiffPIR has two hyperparameters: the regularization scaling $\lambda > 0$, which balances prior and data consistency, and the stochasticity parameter $\zeta \in [0, 1]$, which controls the variance of the reverse step. The latter interpolates between fully deterministic ($\zeta = 0$) and fully stochastic ($\zeta = 1$, analogous to DDPM) sampling. The complete approach is given in Algorithm 2.

Algorithm 2 DiffPIR

Input: Observation \mathbf{y} with noise level σ_y , pre-trained diffusion model $\{\epsilon_\theta, \beta_t, \bar{\alpha}_t\}$ **Hyperparameters:** Stochasticity parameter ζ , regularization strength λ , taken time steps T

- 1: Initialize $\mathbf{x}_T \sim \mathcal{N}(\mathbf{0}, \mathbf{I})$, pre-calculate $\rho_t \triangleq \lambda \sigma_y^2 / \sqrt{(1 - \bar{\alpha}_t) / \bar{\alpha}_t}$
 - 2: **for** $t = T$ **to** 1 **do**
 - 3: $\mathbf{p}_t = (\mathbf{x}_t - \sqrt{1 - \bar{\alpha}_t} \epsilon_\theta(\mathbf{x}_t, t)) / \sqrt{\bar{\alpha}_t}$ ▷ Predict \mathbf{p}_t with score model as denoiser
 - 4: $\hat{\mathbf{x}}_t = \underset{\mathbf{x}}{\operatorname{argmin}} \|\mathbf{A} \mathbf{x} - \mathbf{y}\|^2 + \rho_t \|\mathbf{x} - \mathbf{p}_t\|^2$ ▷ Solving data proximal subproblem
 - 5: $\hat{\boldsymbol{\epsilon}}_t = (\mathbf{x}_t - \sqrt{\bar{\alpha}_t} \hat{\mathbf{x}}_t) / \sqrt{1 - \bar{\alpha}_t}$ ▷ Calculate effective noise
 - 6: $\boldsymbol{\epsilon}_t \sim \mathcal{N}(\mathbf{0}, \mathbf{I})$
 - 7: $\mathbf{x}_{t-1} = \sqrt{\bar{\alpha}_{t-1}} \hat{\mathbf{x}}_t + \sqrt{1 - \bar{\alpha}_{t-1}} (\sqrt{1 - \zeta} \hat{\boldsymbol{\epsilon}}_t + \sqrt{\zeta} \boldsymbol{\epsilon}_t)$ ▷ one step reverse diffusion
 - 8: **end for**
 - 9: **return** \mathbf{x}_0
-

D.3 Variational Reconstruction using Diffusion Models

Following the RED-diff approach [Mardani et al., 2024], we can take Tweedie’s formula (6) and construct the regularizer

$$\mathcal{R}_{\text{RED-diff}}(\mathbf{x}) = \mathbb{E}_{t \sim U[0, T], \boldsymbol{\epsilon} \sim \mathcal{N}(\mathbf{0}, \mathbf{I})} \left[\frac{\sqrt{(1 - \bar{\alpha}_t)}}{\bar{\alpha}_t} \|\boldsymbol{\epsilon}_\theta(\sqrt{\bar{\alpha}_t} \mathbf{x} + \sqrt{1 - \bar{\alpha}_t} \boldsymbol{\epsilon}; t) - \boldsymbol{\epsilon}\|^2 \right]. \quad (10)$$

This regularizer penalizes images \mathbf{x} whose noised versions are poorly denoised by the diffusion model. To solve the induced variational problem (2) using Adam, one requires $\nabla_{\mathbf{x}} \mathcal{R}_{\text{RED-diff}}(\mathbf{x})$. As

shown by Mardani et al. [2024, Prop. 2], we have the tractable expression

$$\nabla_{\mathbf{x}} \mathcal{R}_{\text{RED-diff}}(\mathbf{x}) = \mathbb{E}_{t \sim U[0, T], \epsilon \sim \mathcal{N}(\mathbf{0}, \mathbf{I})} [\lambda_t (\epsilon_\theta(\mathbf{x}_t; t) - \epsilon)], \quad (11)$$

which is analogous to the RED gradient [Romano et al., 2017]. In practice, rather than sampling t in (10) uniformly at random, RED-diff anneals t across the updates. The optimization is initialized at $t = T$ and t is decreased to $t = 0$, mimicking the reverse diffusion trajectory (3). In our implementation, we always use $T = 1000$. For each update, a single $\epsilon \sim \mathcal{N}(\mathbf{0}, \mathbf{I})$ is drawn to approximate the expectation in (11). This schedule regularizes early updates with a coarse prior capturing global structure, while later ones are guided by a finer, low-noise prior that captures detailed features. The weighting scheme λ_t is motivated by the signal-to-noise ratio of the forward process. Recall that the noisy image at time step t can be written as $\mathbf{x}_t = \sqrt{\bar{\alpha}_t} \mathbf{x}_0 + \sqrt{1 - \bar{\alpha}_t} \epsilon$. The authors choose the weighting $\lambda_t = \lambda \sqrt{(1 - \bar{\alpha}_t) / \bar{\alpha}_t}$ with some $\lambda > 0$. The tunable hyperparameters are the regularization strength $\lambda > 0$, the data term scaling γ and the step size for the Adam optimizer. As initialization \mathbf{x}_{init} , we use the FBP for CT and $\mathbf{A}^T \mathbf{y}$ otherwise. The complete approach is given in Algorithm 3. An extension has been recently proposed by Dou et al. [2025].

Algorithm 3 RED-diff

Input: Observation \mathbf{y} , pre-trained diffusion model $\{\epsilon_\theta, \beta_t, \bar{\alpha}_t\}$, initial reconstruction \mathbf{x}_{init}
Hyperparameters: data term scale γ , regularization strength λ , taken time steps T , stepsize Adam

- 1: $\mathbf{x}_T = \mathbf{x}_{\text{init}}$, pre-calculate $\lambda_t \triangleq \lambda \sqrt{(1 - \bar{\alpha}_t) / \bar{\alpha}_t}$
- 2: **for** $t = T$ **to** 1 **do**
- 3: $\epsilon \sim \mathcal{N}(\mathbf{0}, \mathbf{I})$
- 4: $\mathbf{z}_t = \sqrt{\bar{\alpha}_t} \mathbf{x}_t + \sqrt{1 - \bar{\alpha}_t} \epsilon$ ▷ Compute noisy data
- 5: $L_{\mathbf{z}_t}(\mathbf{x}) = \frac{\gamma}{2} \|\mathbf{y} - \mathbf{A}\mathbf{x}\|^2 + \lambda_t (\text{stop_gradient}[\epsilon_\theta(\mathbf{z}_t, t) - \epsilon])^\top \mathbf{x}$
- 6: $\mathbf{x}_{t-1} \leftarrow \text{OptimStep}(\mathbf{x}_t, \nabla L_{\mathbf{z}_t}(\mathbf{x}_t))$
- 7: **end for**
- 8: **return** \mathbf{x}_0

D.4 Latent Space Optimization

In the framework of latent space optimization (LSO) methods [Bora et al., 2017, Duff et al., 2024], we are given a latent model G for the manifold \mathcal{M} . Then, one seeks a reconstruction $\hat{\mathbf{x}} = G(\hat{\mathbf{z}})$ by optimizing the latent code via

$$\hat{\mathbf{z}} \in \arg \min_{\mathbf{z}} \|\mathbf{A}G(\mathbf{z}) - \mathbf{y}\|^2 + \alpha \mathcal{R}(\mathbf{z}), \quad (12)$$

where the regularizer \mathcal{R} ensures that \mathbf{z} remains within high-density regions of the latent space. Representative diffusion-based methods include DMPlug [Wang et al., 2024], BIRD [Chihaoui et al., 2024], and MS-Flow [Denker et al., 2026], where G is commonly implemented using a deterministic sampler such as DDIM [Song et al., 2021]. The memory and computational cost of minimizing (12) scales linearly with the number of the sampling steps. Instead of using an explicit regularizer in (12), Jia et al. [2026] propose to directly optimize over a sphere by introducing the optimizer AdamSphere. The complete approach for DMPlug is given in Algorithm 4. Note that LSO is conceptually related to the Deep Image Prior (DIP) [Ulyanov et al., 2018], where a randomly initialized network is optimized to match the measurements \mathbf{z} . The main hyperparameters of DMPlug are the number of unrolling steps K and the step size of Adam. We follow the choices by Wang et al. [2024] and use $K = 4$ and employ the Adam optimizer. In particular, Wang et al. [2024] employ the early stopping rule by Wang et al. [2021], which was originally designed for the DIP.

E PnP-Flow

Flow matching was introduced by Lipman et al. [2023] and concurrently proposed as rectified flows [Liu et al., 2023] and stochastic interpolants [Albergo and Vanden-Eijnden, 2023]. In the simplest setting, let $X_1 \sim p_1$ denote a data sample and $X_0 \sim p_0 = \mathcal{N}(\mathbf{0}, \mathbf{I})$ a latent variable. Then, given the interpolations $X_t = (1 - t)X_0 + tX_1$, we define the velocity field $v_t(\mathbf{x}) = \frac{1}{1-t} (\mathbb{E}[X_1 | X_t = \mathbf{x}] - \mathbf{x})$, which minimizes the flow matching loss

$$\int_0^1 \mathbb{E}[v_t(X_t) - (X_1 - X_0)] dt.$$

Algorithm 4 DMPlug

Input: Observation \mathbf{y} , pre-trained diffusion model $\{\epsilon_\theta, \beta_t, \bar{\alpha}_t\}$ **Hyperparameters:** Take time steps T , stepsize Adam

```

1:  $\hat{\mathbf{z}} \sim \mathcal{N}(\mathbf{0}, \mathbf{I})$ 
2: function  $G(\mathbf{z})$  ▷ Run deterministic DDIM sampling
3:    $\mathbf{x}_T = \mathbf{z}$ 
4:   for  $t = T$  to 0:
5:      $\hat{\mathbf{x}}_t = (\mathbf{x}_t - \sqrt{1 - \bar{\alpha}_t} \epsilon_\theta(\mathbf{x}_t, t)) / \sqrt{\bar{\alpha}_t}$ 
6:      $\mathbf{x}_{t-1} = \sqrt{\bar{\alpha}_t} \hat{\mathbf{x}}_t + \sqrt{1 - \bar{\alpha}_{t-1}} \epsilon_\theta(\mathbf{x}_t, t)$ 
7:   return  $\mathbf{x}_0$ 
8: end function
9: repeat
10:   $L(\mathbf{z}) = \|\mathbf{A}G(\mathbf{z}) - \mathbf{y}\|^2$  ▷ Compute LSO objective
11:   $\mathbf{z} \leftarrow \text{OptimStep}(\mathbf{z}, \nabla L(\mathbf{z}))$  ▷ Gradient step w.r.t. latent code  $\mathbf{z}$ 
12: until convergence
13: return  $\hat{\mathbf{x}} = G(\hat{\mathbf{z}})$ 

```

In this case, v_t and $p_t := \text{Law}(X_t)$ fulfill the continuity equation $\partial_t p_t + \text{div}(v_t p_t) = 0$. Thus, in order to sample from p_1 , we can sample $\mathbf{x}_0 \sim p_0$ and solve the flow ODE $\dot{\mathbf{x}}_t = v_t(\mathbf{x}_t)$. By the properties of the continuity equation we have (under sufficient regularity) that $\mathbf{x}_1 \sim p_1$, namely an alternative approach of sampling from the data distribution p_1 .

PnP-Flow In order to solve an inverse problem using the velocity v_t of a flow matching model, Martin et al. [2025] interpret $\mathbb{E}[X_1 | X_t = \mathbf{x}] = \mathbf{x} + v_t(\mathbf{x})$ as a (rescaled) denoiser and propose to use it within the forward backward splitting algorithm. Since v_t is trained on images generated by adding noise onto samples from p_1 , an additional interpolation or noise injection step is used. To eliminate the randomness of this noise injection step together with the denoiser, the noise injection and denoising step is averaged over K noise realizations. The full approach is given in Algorithm 5.

Numerically, we observed that PnP-Flow is unstable for small noise levels. As main issue we identified that appropriately large regularization strength γ in the data-fidelity update lead to numerical instabilities. Thus, we replace the explicit gradient step $\mathbf{z}_n = \mathbf{x}_n - \gamma_n \mathbf{A}^T(\mathbf{A}\mathbf{x} - \mathbf{y})$, namely line 4 of Algorithm 5, by an implicit gradient step

$$\mathbf{z}_n = \text{prox}_{\frac{\gamma_n}{2} \|\mathbf{A} \cdot - \mathbf{y}\|^2}(\mathbf{x}_n) = \underset{\mathbf{z}}{\text{argmin}} \left\{ \frac{1}{2} \|\mathbf{z} - \mathbf{x}_n\|^2 + \frac{\gamma_n}{2} \|\mathbf{A}\mathbf{z} - \mathbf{y}\|^2 \right\}. \quad (13)$$

For (13), the solution is given by $\mathbf{z}_n = (\mathbf{A}^T \mathbf{A} + \frac{1}{\gamma_n} \mathbf{I})^{-1} (\mathbf{A}^T \mathbf{y} + \frac{1}{\gamma_n} \mathbf{x}_n)$, which can be computed using the conjugate gradient algorithm (the matrix to be inverted is symmetric and strictly positive definite). The cost of solving the linear system is negligible compared to the evaluation of a large flow model. However, this adaption might be less practical for other data terms or forward models \mathbf{A} that are expensive to evaluate. The PnP-Flow with the implicit gradient steps is given in Algorithm 6. Replacing the explicit gradient step in PnP-Flow with an implicit step was also recently proposed by Flower [Pourya et al., 2026].

Now, we briefly discuss the hyperparameters. We perform $N = 100$ steps for all experiments; taking more did not improve the results. Following Martin et al. [2025], we set the number of noise realizations per step to $K = 5$. Regarding the remaining hyperparameters, we found that $\alpha = 1$ always gives the best results such that we only fit γ . This contrasts Martin et al. [2025], where γ is usually chosen as $\gamma = 1$ and α is fitted by a grid search.

F Experimental Details

In this appendix, we describe the detailed experimental setup for our experiments. We also provide the code at: <https://github.com/alexdenker/GenRegBench>

F.1 Datasets

All datasets are publicly available and briefly described below.

Algorithm 5 PnP-Flow (original)

Input: Observation \mathbf{y} , flow model v_t
Hyperparameters: optimization steps N ,
noise realizations K , scaling exponent α ,
regularization strength γ

- 1: Initialize \mathbf{x}_0 arbitrary
- 2: **for** $n = 0, 1, \dots, N$ **do**
- 3: $t_n = n/N$, $\gamma_n = \gamma(1 - t_n)^\alpha$
- 4: $\mathbf{z}_n = \mathbf{x}_n - \gamma_n \mathbf{A}^T (\mathbf{A} \mathbf{x}_n - \mathbf{y})$
- 5: **for** $k = 1, \dots, K$ **do**
- 6: $\epsilon_{n,k} \sim \mathcal{N}(\mathbf{0}, \mathbf{I})$
- 7: $\tilde{\mathbf{z}}_{n,k} = (1 - t_n)\epsilon_{n,k} + t_n \mathbf{z}_n$
- 8: $\tilde{\mathbf{x}}_{n+1,k} = \tilde{\mathbf{z}}_{n,k} + (1 - t_n)v_{t_n}(\tilde{\mathbf{z}}_{n,k})$
- 9: **end for**
- 10: $\mathbf{x}_{n+1} = \frac{1}{K} \sum_{k=1}^K \tilde{\mathbf{x}}_{n+1,k}$
- 11: **end for**

Algorithm 6 PnP-Flow (implicit gradient step)

Input: Observation \mathbf{y} , flow model v_t
Hyperparameters: optimization steps N ,
noise realizations K , scaling exponent α ,
regularization strength γ

- 1: Initialize \mathbf{x}_0 arbitrary
- 2: **for** $n = 0, 1, \dots, N$ **do**
- 3: $t_n = n/N$, $\gamma_n = \gamma(1 - t_n)^\alpha$
- 4: $\mathbf{z}_n = \text{prox}_{\frac{\gamma_n}{2} \|\mathbf{A} \cdot - \mathbf{y}\|^2}(\mathbf{x}_n)$
- 5: **for** $k = 1, \dots, K$ **do**
- 6: $\epsilon_{n,k} \sim \mathcal{N}(\mathbf{0}, \mathbf{I})$
- 7: $\tilde{\mathbf{z}}_{n,k} = (1 - t_n)\epsilon_{n,k} + t_n \mathbf{z}_n$
- 8: $\tilde{\mathbf{x}}_{n+1,k} = \tilde{\mathbf{z}}_{n,k} + (1 - t_n)v_{t_n}(\tilde{\mathbf{z}}_{n,k})$
- 9: **end for**
- 10: $\mathbf{x}_{n+1} = \frac{1}{K} \sum_{k=1}^K \tilde{\mathbf{x}}_{n+1,k}$
- 11: **end for**

Ellipses The Ellipses dataset consists of synthetic images populated with up to 70 ellipses per sample [Barbano et al., 2022]. For each ellipse, the center location, rotation angle, intensity, and eccentricity are drawn at random. The centers are constrained to lie within a centered circle. We generate the images with a resolution of 256×256 px. We generate 10 000 images for training, 10 for validation and 100 for testing.

Walnut The Walnut dataset [Der Sarkissian et al., 2019] contains 3D CT scans of 42 walnuts. Each scan is a volume of size $501 \times 501 \times 501$ px. From each one, we extract 501 axial slices along the z -axis and discard the first and last 100 slices, as they contain no relevant image content. Since the walnut structure is confined to a central 400×400 px region, we apply a centered crop followed by bilinear interpolation to produce 256×256 px images. We use 41 walnuts for training and the remaining one for testing. The preprocessed dataset is available online³.

AAPM The AAPM dataset comes from the 2016 Low Dose Grand Challenge [McCollough et al., 2017] and contains 10 patient volumes. We follow the setup in DM4CT [Shi et al., 2026] and use the volumes L067, L096, L109, L192, L286, L291, L310 and L333 for training and L506 for testing. The slices have a resolution of 512×512 px, which we downsample to 256×256 px to match the other settings. Every volume is normalized to $[0, 1]$. The data set is available online⁴. We use the B30 reconstruction kernel with full-dose 1 mm slice thickness.

CelebA-HQ The CelebA-HQ dataset [Karras et al., 2018] is a high-resolution version of the CelebA dataset [Liu et al., 2015]. We use the version with 30 000 images of resolution 256×256 px, which is available online⁵. There exists no official split in train, validation and test set. Thus, we randomly selected 10 images for validation and 100 images for testing.

FFHQ/AFHQ The FFHQ [Karras et al., 2019] and AFHQ [Choi et al., 2020] datasets contains photos of human and animal faces, respectively. For AFHQ we use the class cat. We use 100 images for testing and 10 images for validation. The AFHQ dataset and FFHQ datasets are available online⁶. We downsample the images to 256×256 px using Lanczos downsampling.

F.2 Forward Operators

In the following, we describe the forward operators used in this study. All operators are implemented using the `deepinv` library [Tachella et al., 2025].

³https://drive.google.com/drive/u/1/folders/1nhscYxGRUtv50060Ra7221_dSZVb_e7

⁴<https://aapm.app.box.com/s/eaw4jddb53keg1bptavvvd1sf4x3pe9h>

⁵<https://www.kaggle.com/datasets/badasstechie/celebahq-resized-256x256>

⁶<https://huggingface.co/datasets/huggan/AFHQ> and <https://huggingface.co/datasets/marcosv/ffhq-dataset>

Sparse-view tomography. Sparse-view tomography models the acquisition of projection measurements using a Radon transform with a limited number of projection angles. Let $\mathbf{x} \in \mathbb{R}^{H \times W}$ denote the image and R_θ the Radon transform at angle θ . The forward operator is

$$\mathbf{y} = \mathbf{Ax} = \{R_{\theta_i}(\mathbf{x})\}_{i=1}^{N_\theta},$$

where $\{\theta_i\}_{i=1}^{N_\theta}$ are projection angles uniformly distributed over $[0, 180^\circ)$. When N_θ is small, the reconstruction problem becomes severely ill-posed due to insufficient angular sampling.

Inpainting Let $\mathbf{x} \in \mathbb{R}^{CHW}$ denote the (vectorized) ground truth image and $\mathbf{M} \in \{0, 1\}^{HW}$ a fixed binary mask indicating observed locations. The measurement is given by

$$\mathbf{y} = \mathbf{Ax} = \mathbf{M} \odot \mathbf{x},$$

broadcasted across channels. Pixels corresponding to $M_i = 0$ are removed from the observation. In our experiments, the mask is randomly generated with 60% missing pixels and kept fixed across all samples to ensure reproducibility.

Super-resolution Super-resolution is modeled as a low-pass filtering followed by spatial downsampling. The forward operator is

$$\mathbf{y} = \mathbf{Ax} = S(k * \mathbf{x}),$$

where $*$ denotes convolution and S is a uniform subsampling operator with scale factor s and k is a Gaussian filter. We study both $2\times$ and $4\times$ downsampling.

Deblurring Image deblurring is modeled as a spatial convolution with a motion blur kernel. The forward model is

$$\mathbf{y} = \mathbf{Ax} = k * \mathbf{x}$$

where $*$ denotes 2D convolution applied independently to each channel. In our setup, the kernel k is selected as the first motion blur kernel from Levin et al. [2009], which simulates realistic camera motion during exposure.

F.3 Training of Generative Models

Diffusion Models We trained the same architecture with $\approx 80\text{M}$ parameters on `Walnut`, `Ellipses` and `AAPM` using the `diffusers` library [von Platen et al., 2022]. We use the ϵ -matching loss and maintain an exponential moving average for the weights with a decay of 0.999. The learning rate follows a cosine schedule with an initial value of 1×10^{-4} . The batch size is 16. We use a standard DDPM noise schedule with $\beta_0 = 1 \times 10^{-4}$, $\beta_T = 0.02$, and $T = 1000$. The `Ellipses` model is trained for with around 600 000 updates, the `Walnut` model with roughly 1 800 000 updates, and the `AAPM` model with around 1 200 000 updates (training terminates after full batches).

Flow Models In order to train the velocity field used in PnP-Flow, we use the same dataset and architecture as for the score network in the diffusion models. Then, we train with the independent coupling and a batch size of 4 for 200 epochs using the AdamW optimizer with learning rate 1×10^{-4} and exponential decay with factor 0.995. The training code is adapted from Lipman et al. [2024].

F.4 Applying an RGB Diffusion Model to Grayscale Images

Most pre-trained diffusion models are trained on natural RGB images and therefore expect three input channels. However, CT images are inherently grayscale, containing only a single intensity channel. To leverage pre-trained RGB diffusion models, we adopt a simple channel adaptation strategy.

Let $\mathbf{x} \in \mathbb{R}^{1 \times H \times W}$ denote a grayscale image. We construct an RGB compatible input by repeating the grayscale image across channels, i.e., $\mathbf{x}_{\text{RGB}} = [\mathbf{x}, \mathbf{x}, \mathbf{x}]$. The diffusion model then produces a RGB prediction $\hat{\mathbf{x}}_{\text{RGB}} \in \mathbb{R}^{3 \times H \times W}$. We convert the model output back to a single channel by averaging across channels. All data-consistency updates are performed in the grayscale domain. In particular, after predicting $\hat{\mathbf{x}}_{\text{RGB}}$, we average across channels, apply the data-consistency update and then repeat the intensity across the the three channels.

F.5 Hyperparameters

During our experiments, we observed that the hyperparameters suggested for DPS [Chung et al., 2023], DiffPIR [Zhu et al., 2023] and RED-diff [Mardani et al., 2024] are suboptimal for the CT setting. In particular, we often require significantly stronger data consistency, which in turn often also requires more steps in the diffusion sampling process (which of course leads to higher evaluation times). For all methods, we search for the relevant hyperparameters via a grid search on the validation set, see Table 1 for the found values. The search ranges for each hyperparameter are given below.

TV: Regularization strength $\lambda \in \{0.0001, 0.0002, 0.0005, 0.001, 0.002\}$. Minimized with the Condat-Vu primal-dual algorithm [Condat, 2013].

Variational Method PnP-LSR, WCRR and LSR: Regularization strength $\lambda \in \{0.0002, 0.0005, 0.00075, 0.001, 0.002, 0.005, 0.01, 0.02\}$. Minimized with the non-monotonic accelerated gradient descent [Li and Lin, 2015].

DPS: Gradient coefficient $\gamma \in \{0.5, 1, 2, 5, 10, 20\}$; number of steps T is set to 1000 as recommended by Chung et al. [2023].

DiffPIR: stochasticity parameter $\zeta \in \{0.3, 0.5, 0.7\}$; regularization strength $\lambda \in \{0.001, 0.005, 0.01, 0.05, 0.1, 0.5, 1.0, 2.0, 5.0, 7.5\}$; number of steps T is set to 1000 for CT and to 100 for natural imaging.

PnP-flow: Inverse regularization strength $\gamma \in \{200, 500, 1000, 2000, 5000, 10000\}$; scaling exponent $\alpha = 1$ always worked best empirically; we perform $N = 100$ steps for all experiments, taking more did not improve the results further. Following Martin et al. [2025], we set the number K of noise realizations per step to $K = 5$.

RED-diff: regularizer weighting $\lambda \in \{0.01, 0.1, 1.0\}$, data weighting $\gamma \in \{0.1, 0.5, 1.0, 1.25, 1.5, 2.0\}$, step size for Adam $\{0.01, 0.05\}$. We always use $T = 1000$ steps in descending direction, as proposed by Mardani et al. [2024].

DMPlug: We use $K = 4$ unrolling steps and use the early stopping technique with the Adam optimizer as proposed by Wang et al. [2024]. We set the maximum iteration budget to 1500 gradient steps with a step size of 0.01 for the Adam optimizer.

Table 8: Hyperparameters used for CT reconstruction with additive Gaussian noise ($\sigma_n = 0.01$). These maximize the PSNR on a validation set. For TV, PnP-LSR, WCRR and LSR, we have the hyperparameter λ ; for DiffPIR (ζ, λ); for DMPlug (maximum number of steps, number of unrolling iterations, learning rate); for DPS (γ , number of steps); for RED-diff (γ, λ, lr); and for PnP-flow (γ, α , number of steps).

Method	Walnut \rightarrow Walnut (in-distribution)			
	Sparse View (16 angles)	Sparse View (32 angles)	Sparse View (64 angles)	Sparse View (128 angles)
TV	(0.0005)	(0.0005)	(0.0005)	(0.0005)
PnP-LSR	(0.1)	(0.1)	(0.005)	(0.005)
WCRR	(0.01)	(0.005)	(0.005)	(0.005)
LSR	(0.002)	(0.005)	(0.005)	(0.005)
DiffPIR	(0.7, 0.5)	(0.7, 1.0)	(0.7, 1.0)	(0.7, 2.0)
DMPlug	(1500, 4, 0.01)	(1500, 4, 0.01)	(1500, 4, 0.01)	(1500, 4, 0.01)
DPS	(1, 1000)	(10, 1000)	(10, 1000)	(10, 1000)
RED-diff	(1.5, 0.01, 0.05)	(0.75, 0.01, 0.05)	(0.5, 0.01, 0.05)	(0.5, 0.01, 0.01)
PnP-Flow	(1000, 1.0, 100)	(500, 1.0, 100)	(500, 1.0, 100)	(500, 1.0, 100)

F.6 Compute Resources

We launched each training and evaluation routine on a single consumer GPU (depending on the experiment, we used NVIDIA GeForce RTX 4090, NVIDIA Quadro RTX 6000 and NVIDIA GeForce GTX 1080 Ti). The runtime comparison in Figure 4 was done on a NVIDIA GeForce RTX 4090. The training of the compared models took up to two days, the evaluation on a test set with 100 images up to two hours (despite DMPlug, which takes longer).